Deformation associated with the denudation of mantle-derived rocks at the Mid-Atlantic Ridge 13°-15°N: The role of magmatic injections and hydrothermal alteration

Suzanne Picazo, Mathilde Cannat, Adélie Delacour, Javier Escartin, Stéphane Rouméjon, Sergei Silantyev

HAL Id: insu-01827705
https://insu.hal.science/insu-01827705

Deformation associated with the denudation of mantle-derived rocks at the Mid-Atlantic Ridge 13°–15°N: The role of magmatic injections and hydrothermal alteration

Suzanne Picazo and Mathilde Cannat

Equipe de Géosciences Marines, Institut de Physique du Globe de Paris, Sorbonne Paris Cité, Université Paris Diderot, UMR7154 CNRS, 1, rue Jussieu, FR-75238 Paris CEDEX 05, France (picazo@ipgp.fr; cannat@ipgp.fr)

Adélie Delacour

Géosciences Environnement Toulouse, Observatoire Midi–Pyrénées and Université Paul Sabatier, UMR5563, 14 avenue E. Belin, FR-31400 Toulouse, France (adelie.delacour@get.obs–mip.fr)

Javier Escartín and Stéphane Rouméjon

Equipe de Géosciences Marines, Institut de Physique du Globe de Paris, Sorbonne Paris Cité, Université Paris Diderot, UMR7154 CNRS, 1, rue Jussieu, FR-75238 Paris CEDEX 05, France (escartin@ipgp.fr; roumejon@ipgp.fr)

Sergei Silantyev

Vernadsky Institute of Russian Academy of Sciences, Kosygin st., 19, 119991 Moscow, Russia (silantyev@geokhi.ru)

[1] Outcrops of deeply derived ultramafic rocks and gabbros are widespread along slow spreading ridges where they are exposed in the footwall of detachment faults. We report on the microstructural and petrological characteristics of a large number of samples from ultramafic exposures in the walls of the Mid-Atlantic Ridge (MAR) axial valley at three distinct locations at lat. 13°N and 14°45′N. One of these locations corresponds to the footwall beneath a corrugated paleo-fault surface. Bearing in mind that dredging and ROV sampling may not preserve the most fragile lithologies (fault gouges), this study allows us to document a sequence of deformation, and the magmatic and hydrothermal history recorded in the footwall within a few hundred meters of the axial detachment fault. At the three sampled locations, we find that tremolitic amphiboles have localized deformation in the ultramafic rocks prior to the onset of serpentinization. We interpret these tremolites as hydrothermal alteration products after evolved gabbroic rocks intruded into the peridotites. We also document two types of brittle deformation in the ultramafic rocks, which we infer could produce the sustained low magnitude seismicity recorded at ridge axis detachment faults. The first type of brittle deformation affects fresh peridotite and is associated with the injection of the evolved gabbroic melts, and the second type affects serpentinized peridotites and is associated with the injection of Si-rich hydrothermal fluids that promote talc crystallization, leading to strain localization in thin talc shear zones. We also observed chlorite + serpentine shear zones but did not identify samples with serpentine-only shear zones. Although the proportion of magmatic injections in the ultramafic rocks is variable, these characteristics are found at each investigated location and are therefore proposed as fundamental components of the deformation in the footwall of the detachment faults associated with denudation of mantle-derived rocks at the MAR.

1. Introduction

[2] The denudation of mantle-derived ultramafic rocks and gabbros is widespread along slow and ultraslow spreading ridges [*Cannat et al.*, 1992, 2006; *Dick*, 1989; *Karson et al.*, 1987]. This denudation is locally associated with corrugated surfaces, which are interpreted as unroofed axial detachment fault surfaces [*Cann et al.*, 1997; *Dick et al.*, 2008; *Ildefonse et al.*, 2007; *MacLeod et al.*, 2002, 2009; *Tucholke et al.*, 1998]. Denudation of mantle-derived ultramafic rocks and gabbros also occurs in regions of the seafloor that do not show corrugations. In fact, this is the most common case along the Mid-Atlantic Ridge (MAR), with ultramafic and gabbroic outcrops forming the slopes of non-corrugated inside corner massifs next to axial discontinuities [*Cannat and Casey*, 1995; *Dick et al.*, 2008; *Gràcia et al.*, 2000; *Mével et al.*, 1991]. In some regions of slow and ultraslow ridges, ultramafic and gabbroic rocks also crop out extensively along the ridge, away from axial discontinuities [*Cannat et al.*, 2006; *Dick et al.*, 2003; *Escartín et al.*, 2008a]. This is the case in the 13°–15°N region of the MAR, where outcrops of serpentinized peridotites with gabbroic intrusions have been explored by submersible, dredged or drilled up to 80 km from a transform offset [*Cannat et al.*, 1997; *MacLeod et al.*, 2009; *Schroeder et al.*, 2007]. The relief associated with the denudation of ultramafic rocks at mid-ocean ridges is also variable. Actively forming corrugated surfaces at the MAR near 13°N emerge at a very low angle (in some cases less than 4° [*Smith et al.*, 2006]). Paleomagnetic studies indicate that such low angles of fault emergence result from large rotations of the detachment footwall [*Garcés and Gee*, 2007; *MacLeod et al.*, 2011; *Morris et al.*, 2009]. Non-corrugated ultramafic and gabbroic outcrops typically form in ridge regions where the axial valley wall is steeper (>15°), suggesting that the detachment fault there emerged at a higher angle [*Cannat et al.*, 2009].

[3] This diversity in the settings of exhumed mantle-derived ultramafic rocks and gabbros at mid-ocean ridges raises questions as to the mechanics of axial detachment fault systems. In this paper we will specifically examine whether the diversity of denudation settings can be linked with differences in the lithology of the fault and footwall. It has for example been proposed that the angle of emergence of detachment faults could be a function of strain weakening within the footwall material [*Cannat et al.*, 2009]. Thermomechanical models of faulting at slow spreading ridges provide constraints to address these questions. They suggest that the formation of very large offset normal faults or detachments is possible in a relatively thick axial lithosphere if the strength of the fault zone decreases as a function of strain [*Lavier et al.*, 1999, 2000]. Models also suggest that very large offset detachments form when magmatic accretion accommodates 50% or less of plate spreading [*Buck et al.*, 2005; *Tucholke et al.*, 2008]. These predictions can be tested through geological observations and the study of rock samples from mid-ocean ridge detachment faults.

[4] Studies of rocks drilled and dredged within a few tens of meters below exposed corrugated surfaces in the Atlantic [*Boschi et al.*, 2006a; *Escartín et al.*, 2003; *Schroeder and John*, 2004] have indeed indicated significant strain weakening associated with the synkinematic growth of weak hydrous minerals (serpentine, amphibole, chlorite and talc). The growth of Si and/or Al-rich minerals (i.e.,
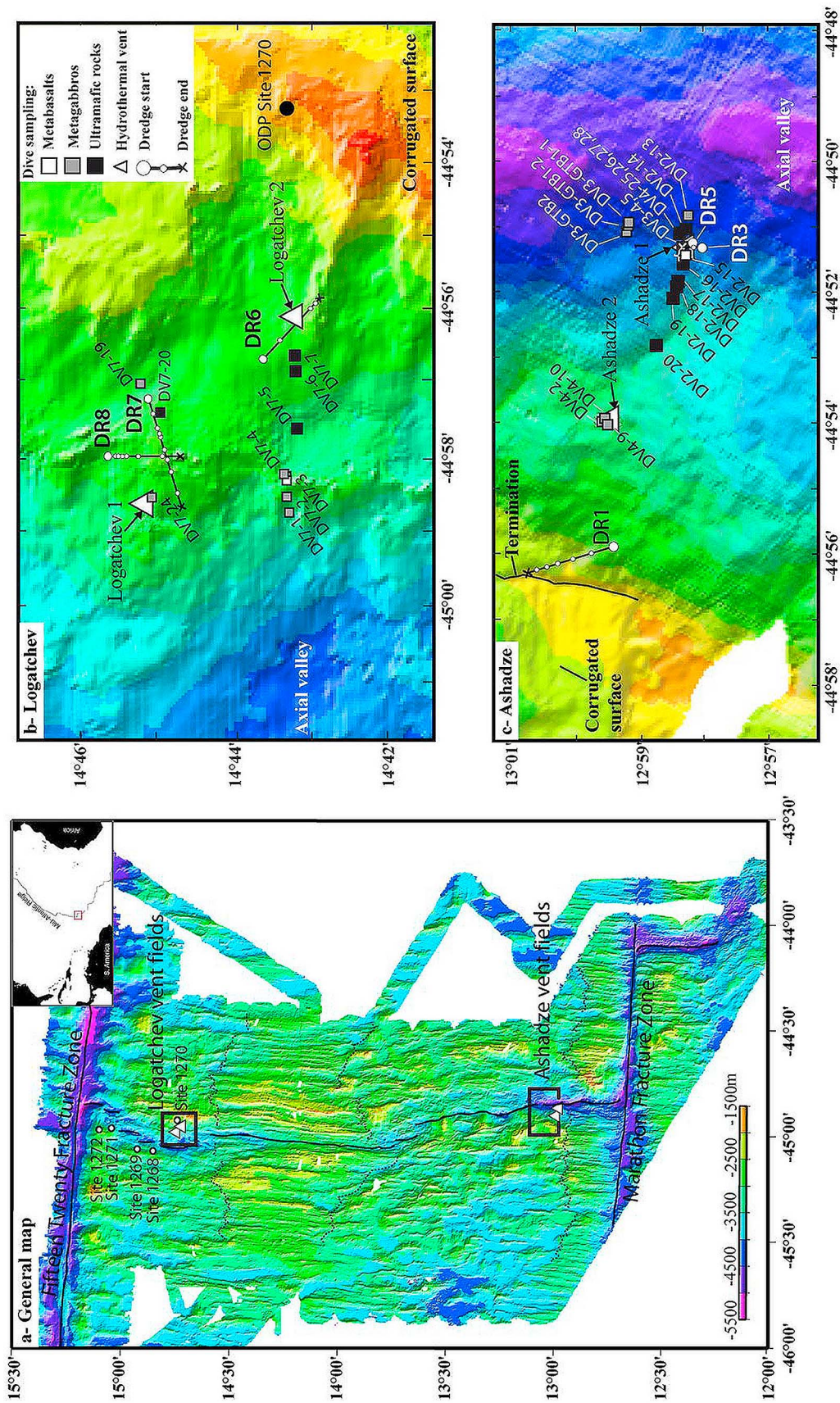
Figure 1

Table 1. Localization and Length of the Serpentine Cruise Dredge Hauls Based on On-Bottom/Off-Bottom Positions, Recalculated From Ship Position, Wire-Out Values, and Local Bathymetry[a]

Lat. N, Start	Long. E, Start	Depth (m), Start	Lat. N, End	Long. E, End	Depth (m), End	Length (m)	Weight (kg)	Total Number of Samples
12°59.70′	−44°56.40′	−2364	13°00.00′	−44°57.00′	−2254	775	300	130
12°58.32′	−44°51.60′	−3971	12°58.38′	−44°51.60′	−4000	260	50	43
12°58.44′	−44°51.60′	−4000	12°58.62′	−44°52.20′	−3950	346	1000	36
14°43.68′	−44°56.40′	−2835	14°42.90′	−44°55.80′	−2547	1820	90	59
14°45.18′	−44°57.00′	−2796	14°44.94′	−44°58.14′	−2681	1745	70	26
14°45.54′	−44°58.20′	−2830	14°44.70′	−44°58.20′	−2718	1567	1000	148

[a]Weight of each dredge was estimated on board, and a total of 470 samples were numbered as a function of rock type.

amphibole, chlorite and talc) indicates that a gabbroic component was added to the primarily ultramafic material in the fault zone. This gabbroic component has been interpreted either as altered magmatic intrusions [*Boschi et al.*, 2006a; *Schroeder and John*, 2004], or as introduced by metasomatic hydrothermal fluids [*Escartín et al.*, 2003]. Non-corrugated ultramafic outcrops in the axial valley walls probably expose the footwall of detachment faults, a few tens to a few hundred meters below the actual fault, that would have been eroded by landslides [*Cannat et al.*, 2010; *Mitchell et al.*, 2000; *Searle et al.*, 1998]. Previously published studies of such sample sets indicate variable degrees of brittle, semi-brittle and plastic overprint of the original asthenospheric fabric of the peridotites, from pervasively crushed serpentinites exposed in the western axial valley wall at 15°30′N on the MAR [*Cannat et al.*, 1997], to massive serpentinized peridotites with quasi intact asthenospheric fabrics [*Ceuleneer and Cannat*, 1997] at ODP Site 920 near 23°20′N. This variability has not until now attracted much attention, the focus being put on the detachment fault zones in places where they could unambiguously be sampled, i.e., in corrugated terranes. Yet, documenting the diversity of deformation types in footwall rocks may be key to understanding the mechanisms that control denudation processes and their variability.

[5] In this paper, we analyze deformation structures that we infer are related to the denudation of ultramafic

and associated gabbroic rocks and metabasalts on the walls of the Mid-Atlantic Ridge axial valley at latitudes 13°N (next to the ultramafic-hosted Ashadze vent field), and 14°45′N (next to the Logatchev vent field; Figure 1). These samples were dredged and sampled by ROV during the SERPENTINE cruise with the R.V. Pourquoi Pas? in 2007 [*Charlou et al.*, 2010]. One of these dredges (DR1) sampled the footwall of a sub-horizontal fossil corrugated surface that forms the top of the axial valley wall at 13°N (Figure 1c). The other 5 dredges (DR3, DR5, DR6, DR7, DR8; Figures 1b and 1c and Table 1), and all of the ROV dives sampled uncorrugated ultramafic terranes in the Ashadze or Logatchev regions. All the sampled regions show clear evidence of mass-wasting [*Cannat et al.*, 2010; *Petersen et al.*, 2009], suggesting that the sampled material comes from beneath the main fault surface. Our approach is to compare these corrugated and non-corrugated settings and the two sampled areas (Ashadze and Logatchev), by systematically relating deformation structures to rock type, and to characteristics of hydrothermal alteration.

[6] Although we do briefly describe deformation structures in magmatic (gabbroic and basaltic) lithologies, we focus our study on deformation that affects the residual ultramafic lithologies in our sample set, because these lithologies have experienced tectonic denudation and progressive cooling throughout the full thickness of the axial lithosphere. In these ultramafic rocks, it is therefore

Figure 1. Regional setting of the studied samples. (a) Bathymetry of the Mid-Atlantic Ridge between the Fifteen-Twenty Fracture Zone and the Marathon Fracture Zone [after *Smith et al.*, 2008]. Thin dashed lines contour regions of the seafloor with regular abyssal hills, interpreted as more volcanic. Frequent outcrops of mantle-derived peridotites and gabbros, and corrugated surfaces are observed in the intervening seafloor regions. Boxes correspond to the areas of Figures 1b and 1c, open triangles to the location of the Logatchev and Ashadze hydrothermal vent fields and open circles to ODP Leg 109 drill sites. (b) The Logatchev area on the east wall of the axial valley, with location of our dredged and ROV samples. (c) The Ashadze area, in the west wall of the axial valley, with location of our dredged and ROV samples. Closed circles and crosses along dredge haul tracks represent the recalculated positions for dredge touch down and off bottom, and for the principal peaks in cable tension along the track (smaller closed circles). These positions were recalculated based on ship position, wire-out values, and local bathymetry. Note that DR1 samples the cliff below a fossil corrugated surface, close to the termination of the detachment fault.

possible to interpret the deformation styles and the associated metamorphic facies in terms of depth with respect to significant horizons such as the base of the brittle axial lithosphere, or the base of the hydrothermally altered domain. By contrast, magmatic rocks may have been intruded and cooled from their magmatic temperature at any level in the axial lithosphere [*Cannat*, 1996]. Their deformation style and deformed paragenesis are therefore not necessarily diagnostic of specific horizons at the scale of the axial lithosphere.

2. Geological Setting and Previous Sampling of Ultramafic and Gabbroic Rocks in the 13°−15°N Area

[7] The Mid-Atlantic Ridge between 13° and 15°N comprises two regions of seafloor with regular abyssal hills and negative gravity anomalies, interpreted as volcanically robust segments [*Smith et al.*, 2008]: one between the Marathon Fracture Zone and 13°N, and the other between 13°50′N and 14°30′N (Figure 1a). The seafloor between these two volcanically robust regions, and between 14°30′N and the Fifteen-Twenty Fracture Zone is characterized by blocky or rugged seafloor [*Cannat et al.*, 1997; *Escartín and Cannat*, 1999; *Fujiwara et al.*, 2003; *Smith et al.*, 2008], frequent ultramafic outcrops, and a high density of domal and commonly corrugated bathymetric features interpreted as core complexes [*Smith et al.*, 2008]. This second type of terrane represents nearly 50% of the seafloor accreted during the past 10 Myrs [*Smith et al.*, 2008]. This is substantially more than observed elsewhere along the Mid-Atlantic Ridge: for example in the Kane Fracture Zone region (23°N) the estimated proportion of seafloor with frequent ultramafic and gabbroic outcrops is 25% [*Cannat et al.*, 1995]. This makes the 13°−15°N MAR region one of the best natural laboratories to study detachment fault processes at mid-ocean ridges.

[8] Outcrops of serpentinized peridotites in the 13°−15°N MAR region were first sampled next to the Fifteen Twenty Fracture Zone [*Rona et al.*, 1987]. More detailed geological studies followed based on a Nautile submersible cruise in 1992 [*Bougault et al.*, 1993; *Cannat et al.*, 1997; *Cannat and Casey*, 1995]. Numerous dredging cruises then led to the collection of more ultramafic samples [*Silantyev*, 1998], and to the discovery of the ultramafic-hosted Logatchev [*Batuev et al.*, 1994] and Ashadze [*Bel'tenev et al.*, 2005; *Cherkashov et al.*, 2008] hydrothermal vent fields (Figure 1).

More detailed investigations and sampling of these ultramafic outcrops included drilling at ODP Leg 209 Sites 1268, 1270, 1271, and 1272 [*Kelemen et al.*, 2007] (Figure 1), ROV observations in the Logatchev area [*Augustin et al.*, 2008; *Petersen et al.*, 2009], and side scan imaging and sampling of the emerging corrugated surfaces at 13°20′N [*MacLeod et al.*, 2009].

[9] Of all the samples available prior to our study, only those from ODP Leg 209 Site 1270 come from a clearly corrugated surface [*Garcés and Gee*, 2007]. The other drilled and dredged samples come from outcrops of exhumed ultramafic rocks or gabbros along the axial valley walls, or from domal, yet un-corrugated structures next to the Fifteen Twenty Fracture Zone [*Schroeder et al.*, 2007] and near the Logatchev vents [*Petersen et al.*, 2009]. Paleomagnetic indications of large tectonic rotations consistent with emplacement by axial detachment faults are reported for ultramafic rocks drilled at ODP Leg 209 Sites 1268 (non corrugated outcrops) and 1270, while paleomagnetic data from Sites 1271 and 1272 are described as inconclusive [*Garcés and Gee*, 2007].

[10] In terms of deformation that could be related to denudation, previous studies in the 13°N–15°N area include reports of brittle-plastic deformation of gabbroic dikes and veins in ultramafic samples next to the Fifteen Twenty Fracture Zone [*Cannat and Casey*, 1995], and studies of more extensively deformed samples from ODP Leg 209 [*Jöns et al.*, 2009; *Schroeder et al.*, 2007]. Ultramafic rocks drilled at ODP Sites 1268, 1270, 1271 and 1272 (Figure 1) display 3 deformation facies: 1- high temperature plastic mylonites with recrystallization of primary olivine and pyroxene are found at Site 1268 next to a decameter-sized gabbroic intrusion, and crop out near ODP Site 1270, (dive 425, MODE98 cruise [*Kelemen et al.*, 1998]); 2- serpentine, amphibole and chlorite-bearing schists interpreted as sheared metagabbroic [*Schroeder et al.*, 2007] and plagiogranitic [*Jöns et al.*, 2009] veins in peridotites are found at ODP Sites 1270 and 1271, and 3- meter-sized intervals of cataclastic serpentine breccias and gouge have been recovered at ODP Sites 1270, 1271 and 1272 [*Schroeder et al.*, 2007].

3. Sample Locations and Lithological Descriptions

[11] Our sample set comprises 470 samples collected by dredging (442 samples; Table 1) and along ROV Victor dives (28 samples) in the

Table 2. Lithological Types Identified in Our Set of 470 Rock Samples and Their Relative Abundances in Terms of Number of Samples, Number of Studied Thin Sections, and Volume % in Each Dredge[a]

Lithology	Lithology Type	Number of Samples	Number of Thin Sections	DR1 (vol. %)	DR3 (vol. %)	DR5 (vol. %)	DR6 (vol. %)	DR7 (vol. %)	DR8 (vol. %)
Basalts	1	27	–	15.9	–	–	–	–	1.6
Metabasalts	2a	26	–	26.6	–	–	–	–	–
Metabasalts with leucocratic injections	2b	12	3	11.9	–	–	–	–	–
Metagabbro	3a	100 + 1 (p)	13 + 1 (p)	5.9	5.4		24.7	49.3	26.9
Metagabbro with leucocratic injections	3b	19	9	4.1			1.7	–	–
Leucocratic magmatic rocks	3c	11	1	3.1	–	–	–	–	–
Serpentinized peridotite	4a	114 + 8 (v)	46 + 4 (v)	–	81.4	91.1 + 5 (v)	51.6 + 0.7 (v)	35.0	20.0 + 7.1 (v)
Amphibole and/or chlorite-bearing serpentinized peridotite	4b	87 + 16 (p)	56 + 7 (p)	25.6	6.5 + 0.1 (p)	3.4	15.3	13.5	12.4 + 18.8 (p)
Talc-bearing amphibole and chlorite free serpentinized peridotite	4c	46	14	6.8	6.5	0.4	0.7	2.1	13.0
Quartz-bearing hydrothermal rocks	5	3	2	–	–	–	5.2	–	–
Total		470	156	100	100	100	100	100	100

[a]These volume proportions are based on shipboard measurements of the size of each sample. Note that DR1 (sampling the cliff below a fossil corrugated surface; Figure 1) contains the largest proportion of basaltic samples (lithological types 1 and 2), while ultramafic lithologies make up more than 94% of the volume of rocks recovered in DR3 and DR5 (sampling the vicinity of the Ashadze 1 vent field). p: polygenic brecci; v: with gabbroic veins.

vicinity of the Ashadze and Logatchev hydrothermal vent fields (Figure 1). These 470 rock samples were first described on board and named as follows: SE for the SERPENTINE cruise, then the dredge or dive number DR1/DV1, then for dredged samples, the lithological type number, and the sample number. For our study, we selected 156 representative samples for thin section observations. Sections were, whenever applicable, cut perpendicular to the foliation and parallel to the lineation of the sample. Optical microscopy then allowed us to refine the shipboard descriptions and to define 10 lithologies (Table 2). Table S2 in the auxiliary material lists all the samples and their lithology.[1] For samples for which we do not have a thin section, the lithology is inferred based on the microscopic observation of macroscopically similar samples.

[12] The 10 lithologies identified in our sample set are: basalt, metabasalt, metabasalt with leucocratic injections, metagabbro, metagabbro with leucocratic injections, leucocratic magmatic rocks or plagiogranites, serpentinized peridotite (some with gabbroic veins), amphibole and/or chlorite-bearing serpentinized peridotite, with or without talc, talc-bearing amphibole and chlorite-free serpentinized peridotite, and quartz-bearing hydrothermal rocks. Geochemical data for some of these lithologies may be found in *Silantyev et al.* [2011]. The relative proportions of each lithology in the 6 studied dredges are estimated based on sample volume and shown in Table 2. Gabbroic lithologies are most abundant (49%) in DR7 next to the Logatchev vents, and basaltic and metabasaltic rocks dominate (54.4%) in DR1 beneath a fossil corrugated surface west of the Ashadze vents (Figure 1c). Rocks from DR3 and 5 next to the Ashadze 1 vent field are almost exclusively ultramafic (≥94.6%).

[13] Gabbroic rocks (lithological types 3a, b and c) are variably altered into secondary amphibole-chlorite assemblages and therefore classified broadly as metagabbros. Their inferred protoliths include coarse-grained gabbros and finer grained oxide and/or amphibole-bearing gabbros, with irregular patches of leucocratic, zircon-bearing material (DR1, Figures 2a and 3a). Ultramafic rocks (lithological types 4a, b and c) are extensively altered into serpentine or talc (only 46 out of our 130 ultramafic thin sections contain olivine relicts). The composition of relicts of the primary peridotite mineralogy (olivine, orthopyroxene, uncommon clinopyroxene, and spinel; Table S4) is consistent with a depleted
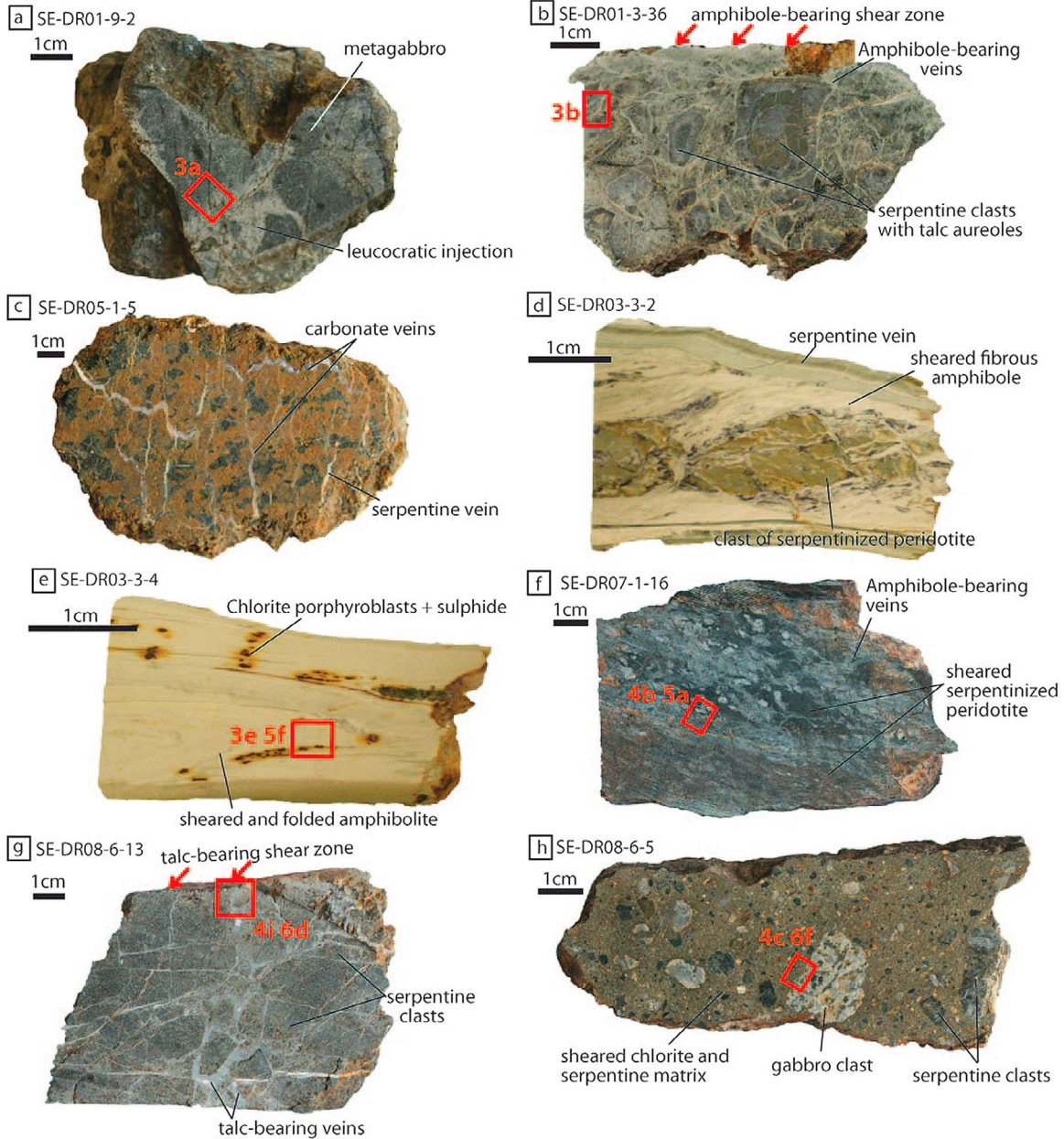
Figure 2. Photographs of selected ultramafic and metagabbroic samples. Sample number is shown in upper left and red squares show the emplacement of photomicrographs shown in Figures 3–6. DR1, DR3 and DR5 samples come from the Ashadze region and DR6, DR7 and DR8 samples come from the Logatchev region. (a) Lithological type 3b: metagabbro (dark gray) with injections of zircon-bearing leucocratic material. (b) Lithological type 4b: amphibole and chlorite-bearing serpentinized peridotite. Ultramafic clasts in a lighter amphibole-bearing matrix are partially replaced by talc. The upper face of the sample is a 0.5 cm-thick amphibole-bearing shear zone. (c) Lithological type 4a: serpentinized peridotite. This sample contains array of carbonate veins. (d) Lithological type 4b: amphibole and chlorite-bearing serpentinized peridotite. Green clasts of serpentinized peridotite in lighter matrix of sheared amphibole. Two sub-parallel faces of sample correspond to later crack-seal serpentine veins. (e) Lithological type 4b: amphibole-schist with folds and sulphide-bearing chlorite porphyroblasts. (f) Lithological type 4b: amphibole and chlorite-bearing serpentinized peridotite. Heterogeneous plastic deformation of peridotite produces coarse foliation, underlined by amphibole and chlorite-rich domains in gray. (g) Lithological type 4c: talc-bearing serpentinized peridotite. Clast-supported breccia made of angular clasts of serpentinized peridotite, locally replaced by talc, and separated by an angular network of talc veins. The upper face of the sample corresponds to a thin talc-bearing shear zone. (h) Lithological type 4b: amphibole and chlorite-bearing serpentinized peridotite. Matrix-supported breccia made of angular to sub-angular clasts of serpentinized peridotite and metagabbro in a sheared chlorite, talc and serpentine matrix.

residual harzburgitic protolith [*Silantyev et al.*, 2011].

3.1. The Ashadze Region

[14] The two Ashadze hydrothermal vent fields are located on the western axial valley wall of the Mid-Atlantic Ridge at lat. 13°N (Figure 1c). During the Serpentine cruise, the area next to these vents was sampled during 3 ROV VICTOR dives (SE-DV 311, 312 and 313), and 3 successful dredges (DR1, DR3, and DR5). The map distribution of rock types for the dive samples shows that outcropping lithologies are dominantly ultramafic next to the Ashadze 1 vents, and that metagabbros are common next to the Ashadze 2 vents (Figure 1c).
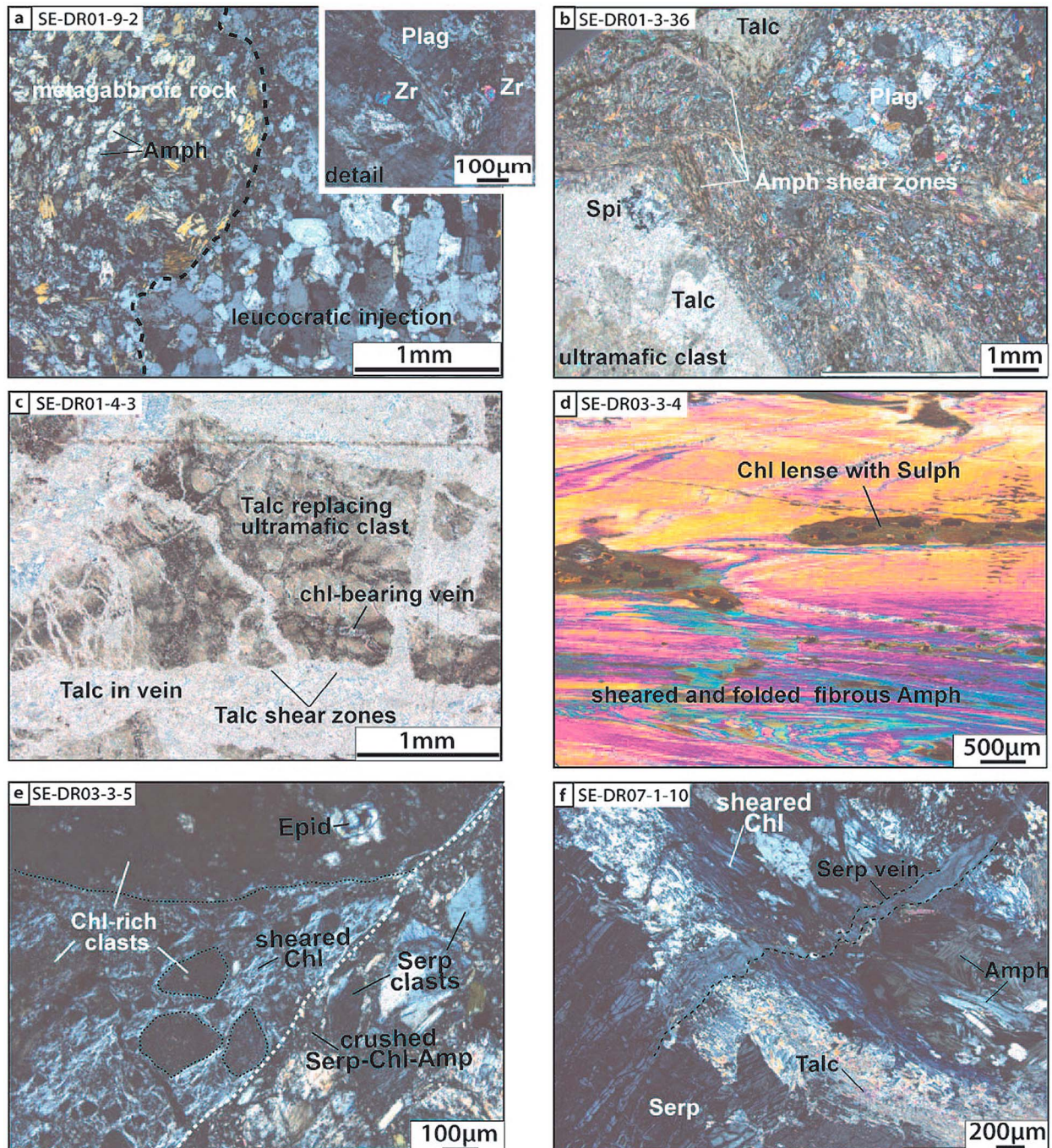

Figure 3

[15] DR1 (estimated weight of recovered rocks 300 kg; 130 samples; Table 1) sampled a steep scarp that cuts into the footwall of a fossil corrugated surface (Figure 1c). The dredge haul explored this scarp 350m to 100m below the corrugated surface. Because dredged lithologies could represent talus, we can only be sure that our samples come from less than 350m below the corrugated fault surface. The dredged lithologies (Table 2) include unmetamorphosed basalts (15.9%), and a suite of metamorphic rocks both mafic (51.6%) and ultramafic (32.4%) in composition. All of the ultramafic samples in this dredge contain talc, or amphibole, or both. Amphibole and/or chlorite-bearing serpentinized peridotites (25.6% in volume of the whole dredge; Table 2) are made of angular clasts of serpentinized peridotite in an amphibole-rich matrix (Figures 2b and 3b). This matrix also commonly contains chlorite and zircon and occasionally relicts of plagioclase (Figure 3b). Talc develops as a replacement mineral in the ultramafic rocks, forming millimeter to centimeter-thick metamorphic aureoles next to the amphibole-bearing material (Figure 3b). In some samples, talc also fills angular crosscutting veins (Figure 3c), and grows as a static replacement of the serpentine meshwork.

[16] DR3 and DR5 (Table 1) sampled the lower slopes of the axial valley wall near the Ashadze 1 vents (Figure 1c). DR3 recovered only 50 kg of rocks (43 samples), but DR5 recovered almost 1 ton of quite homogeneous ultramafic rocks of which only 36 samples were selected for study. Talc, chlorite and amphibole-free serpentinized harzburgites are the dominant lithology in both dredges (81.4 and 96.1% in volume respectively; Table 2).

They are green or orange in color and commonly contain veins of serpentine or carbonate (Figure 2c). In some samples, these veins are close-spaced and associated with limited brittle deformation of the ultramafic rocks. Amphibole and/or chlorite-bearing serpentinized peridotites, most of which are talc-free, form only 6.6% in volume of DR3 and 3.4% of DR5. Amphiboles occur in veins and in irregular patches surrounding clasts of serpentinized peridotite (Figure 2d). Most of these amphibole-bearing samples are deformed by amphibole-bearing shear zones. These shear zones are locally cut by serpentine veins. Samples of extensively sheared and folded amphibolite with sulphide-bearing chlorite porphyroblasts were also recovered (Figures 2e and 3d). DR3 also includes one sample of a breccia with decimeter to sub-millimeter-sized angular clasts of serpentinized peridotite and of a zircon and epidote-bearing chlorite-rich material, in a sheared chlorite and serpentine-bearing matrix (Figure 3e). Talc-bearing, amphibole and chlorite-free serpentinized peridotites (lithological type 4c) represent only 6.5% in volume of DR3 and 0.4% of DR5 (Table 2). Talc in these samples fills angular crosscutting veins, or grows as a static replacement of the serpentine meshwork, similar to talc-bearing type 4b and c samples in DR1 (Figure 3c). DR3 also contains a few samples of metagabbro (5.4% in volume). Gabbroic rocks in DR5 only occur as rare millimeter to centimeter-thick veins in serpentinized peridotites.

3.2. The Logatchev Region

[17] The two Logatchev hydrothermal vent fields are located to the east of the Mid-Atlantic Ridge

Figure 3. Photomicrographs of selected ultramafic and metagabbroic samples (polarized light). Sample number is shown in upper left. DR1, DR3 and DR5 samples come from the Ashadze region and DR6, DR7 and DR8 samples come from the Logatchev region. Abbreviations: plagioclase (Plag), amphibole (Amph), zircon (Zr), chlorite (Chl), serpentine (Serp), spinel (Spi), and sulphide (Sulph). (a) Metagabbro with leucocratic injections (lith. type 3b; see sample in Figure 2a). Leucocratic material with rectangular plagioclase, zircons (inset) and rare fibrous amphiboles is injected in crudely foliated metagabbroic rock with plagioclase and prismatic amphibole. (b) Amphibole and chlorite-bearing serpentinized peridotite (lith. type 4b; see sample in Figure 2b and more detailed photomicrograph in Figure 5c). Angular clasts of serpentinized peridotite are extensively replaced by talc in an amphibole-rich, plagioclase-bearing matrix. Thin shear zones are underlined by amphibole. (c) Amphibole and chlorite-bearing serpentinized peridotite (lith. type 4b). Angular clasts of serpentinized peridotite are extensively replaced by talc, and cut by talc and chlorite-bearing veins in a matrix of talc and minor chlorite, with ≤50 μm-thick talc-bearing shear zones. (d) Amphibole-schist with folds and elongated sulphide-bearing chlorite porphyroblasts (lith. type 4b; see sample in Figure 2e and SEM image in Figure 5f). (e) Polygenic breccia with chlorite-rich, epidote-bearing clast in a matrix of sheared chlorite and serpentine (lith. type 4b). Chlorite dominates in the clasts and in the matrix in the upper left side of the photograph. This chlorite-rich domain is incorporated as a clast of clasts in a cataclastic material made of crushed serpentine, chlorite and minor amphibole (right hand side of the white dashed line). (f) Lithological type 4b: Serpentine vein crosscutting sheared amphibole and chlorite vein in serpentinized peridotite (lith. type 4b). Serpentine vein opened during serpentinization of host peridotite. Talc formed as static replacement next to amphibole-bearing vein.
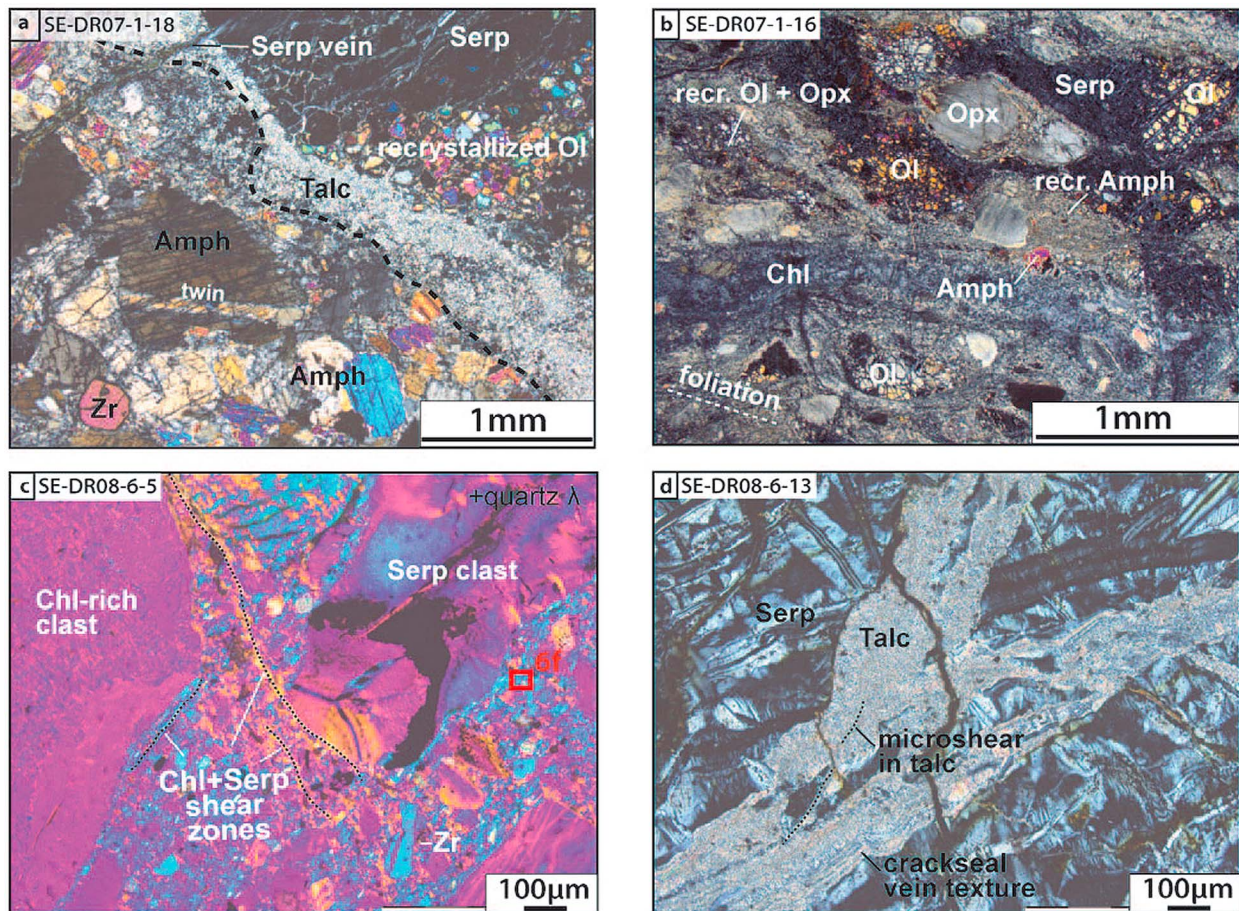
Figure 4. Photomicrographs of selected ultramafic samples. Sample number is shown in upper left. Polarized light, with quarter wave plate in Figure 4c. Abbreviations: amphibole (Amph), zircon (Zr), chlorite (Chl), serpentine (Serp), olivine (Ol), and orthopyroxene (Opx). (a) Contact between partially serpentinized peridotite and amphibole and zircon-bearing vein (lith. type 4b). Note magmatic twin in amphibole. Olivine in peridotite is extensively recrystallized. Talc formed as static replacement next to amphibole-bearing vein, and contact is cut by serpentine vein. (b) Heterogeneous plastic to semi-brittle deformation of olivine and orthopyroxene in amphibole-bearing serpentinized peridotite (lith. type 4b; see sample in Figure 2f and more detailed photomicrograph in Figure 5a). Olivine porphyroclasts show tight subgrain boundaries, orthopyroxenes are kinked and form elongated strings of rounded to angular porphyroclasts. Olivine and orthopyroxene neoblasts underline crude foliation. Chlorite-rich domains in gray are irregular, and discordant to this foliation. (c) Polygenic breccia with clasts of serpentinized peridotite and of a chlorite-rich metagabbroic material (lith. type 4b; see sample in Figure 2h and SEM image in Figure 6f). The quarter wave plate emphasizes the preferred orientation of the optical axis of chlorite and serpentine, underlining array of thin shear zones in the matrix. (d) Clast-supported serpentinite breccia with angular to sub-angular clasts of serpentinized peridotite separated by talc veins, some with crack-seal textures (lith. type 4c; see sample in Figure 2g). Talc also replaces serpentine.

axial valley at lat. 14°45′N (Figure 1b). During the Serpentine cruise, the area surrounding these vents was sampled by ROV VICTOR dive SE-DV316, and by 3 successful dredges (DR6, DR7, and DR8). Figure 1b shows the map distribution of rock types in the dive samples.

[18] DR6 sampled the area next to the Logatchev 2 vent (Figure 1b). It recovered about 90 kg of rocks (59 samples; Table 1). Mafic samples represent 26.4% in volume and comprise variably

metamorphosed gabbros, a few with leucocratic injections. Quartz and sulphide-rich samples with mafic clasts were also recovered and interpreted as fragments of a hydrothermal stockwork [*Silantyev et al.*, 2011]. Ultramafic rocks represent 70.4% in volume of this dredge. Talc, amphibole and chlorite-free serpentinized harzburgites (lithological type 4a) are the dominant lithology (52.3% in volume), with green to pale green samples and reddish samples cut by carbonate veins similar to those in DR3 and

DR5 (Figure 2c). A few of these samples contain millimeter to centimeter-thick gabbroic veins, with coarse chlorite pseudomorphs after plagioclase and no significant deformation. Amphibole and/or chlorite-bearing samples (lithological type 4b) represent 15.3% in volume of the whole dredge (Table 2). Amphibole and chlorite occur in millimeter-thick veins, some of them sheared. These veins, spaced by up to few decimeters, commonly correspond to the outer surface of the ultramafic samples. Talc is present in the ultramafic host next to these veins. Extensive talc replacement with no nearby vein of amphibole and/or chlorite was observed in only one ultramafic sample (SE-DR6-1-30).

[19] DR7 (estimated weight 70 kg; 26 samples) sampled the intermediate slopes of the eastern axial valley wall, to the east and above the Logatchev 1 vent field (Figure 1b). Gabbroic rocks represent 49.3% in volume (Table 2) and comprise moderately metamorphosed medium to fine-grained gabbros and iron oxide-bearing gabbros [*Silantyev et al.*, 2011]. Ultramafic rocks represent 50.7% in volume. As in DR6, talc, amphibole and chlorite-free serpentinized harzburgites (lithological type 4a) are the dominant ultramafic lithology (35% in volume of the whole dredge). Amphibole and/or chlorite-bearing ultramafic samples (lithological type 4b, 13.3% in volume) are similar to those in DR3, showing clasts of partially serpentinized peridotite in a network of amphibole-bearing veins (Figure 4a), or in a sheared amphibole and chlorite-bearing matrix (Figures 2f and 4b). These shear zones are locally cut by serpentine veins (Figure 3f). Serpentinization and talc replacement in these clasts are commonly less than observed in the Ashadze region, preserving the original fabric of the peridotite (Figures 4a and 4b). Similar to the Ashadze samples, talc occurs in metamorphic aureoles around altered peridotite clasts and in angular crosscutting veins (Figure 2g) similar to those observed in some DR1 samples. Only one talc-bearing amphibole and chlorite-free sample (lithological type 4c) was recovered. In this sample talc occurs in crosscutting talc-filled veins, and as local replacement of the serpentine mesh.

[20] DR8 sampled the intermediate slopes of the eastern axial valley wall, next to DR7 and to the east and above the Logatchev 1 vent field (Figure 1b). It recovered almost 1 ton of a wide variety of rock types, of which 148 representative samples were retained (Table 1). Variably metamorphosed gabbroic rocks and a few small blocks of unmetamorphosed basalt represent 28.5% in volume (Table 2). Talc, amphibole and chlorite-free serpentinized peridotites (lithological type 4a) represent 27.1% in

volume. Some of these samples contain undeformed millimeters to centimeter-thick veins of metagabbro with occasional relicts of plagioclase. One sample (DR8-7-5) contains a 5 cm-thick vein of medium to coarse-grained undeformed oxide and zircon-bearing gabbro. Amphibole and/or chlorite-bearing serpentinized peridotites (lithological type 4b) represent 31.2% of the whole dredge volume (Table 2). Many of these type 4b samples resemble amphibole and chlorite-bearing samples in the other dredges, with amphibole and chlorite in veins or in sheared intervals between ultramafic clasts. More than one half of these type 4b samples and 18.8% in volume of the dredge, however, are polygenic sheared breccias (Figure 2h). These breccias contain decimeter to sub-millimeter-sized angular clasts of serpentinized peridotite, gabbro, and oxide-bearing metagabbros, in a sheared chlorite and serpentine-bearing matrix (Figures 2h and 4c). Talc-bearing but amphibole and chlorite free serpentinized peridotites (lithological type 4c, 13% in volume; Table 2) show arrays of talc veins (Figure 4d) and locally pervasive talc replacement of the serpentine mesh.

4. Microstructures and Mineralogy of Deformed Rock Samples

[21] Nearly 50% of the ultramafic samples (127 out of a total of 270; Table 2) display some degree of deformation. For metabasalts, metagabbros, and leucocratic magmatic rocks, this proportion is somewhat lower (about 30% or 49 out of 169 samples), and the unmetamorphosed basalts recovered along dive 311 (Figure 1) and in DR1 and DR8 are undeformed. In this chapter, we report on the characteristics of the deformed samples, based on optical microscopy and Scanning Electron Microscopy (ZEISS SUPRA 55VP SEM at University Pierre et Marie Curie, Paris).

[22] Deformation textures in metagabbros include: 1- a magmatic foliation marked by well oriented plagioclase tablets (observed in only one thin section); 2- a foliation marked by plagioclase, clinopyroxene, and brown amphibole that recrystallized in polygonal grains ~100 μm in size. This plastic deformation texture is observed in most thin sections of fine-grained oxide-bearing metagabbros from DR8 and in two oxide-free metagabbro from DR1; and 3- an episode of heterogeneous plastic deformation, with syn-kinematic growth of fibrous amphibole and incipient recrystallization of plagioclase in grains 10–20 μm in size. This deformation is found in 10 thin sections of metagabbro and leucocratic rocks from DR1, DR3 and DR8. Because magmatic rocks

Table 3. Types of Deformation Identified in the Dredged Ultramafic Samples, as a Function of Lithology (Types 4a, 4b or 4c, as Defined in Table 2)[a]

	Lithology	Total Number of Samples	Total Number of Thin Sections	Thin Sections With Relics of Olivine	Plastic to Semi-brittle 1 Ol + Opx + Amph	Brittle 1 Peridotite	Plastic to Semi-brittle 2 Amph ± Chl	Serpentinization Ribbon Texture	Brittle 2 Serpentine	Plastic to Semi-brittle 3 Tlc ± Chl + Serp ± Carb
DR 1	4a	0	0	—	—	—	—	—	—	—
	4b	21	18	1	—	—	12	—	2 (t)	5 (t)
	4c	19	4	—	—	—	—	—	—	1 (t)
DR3 and DR 5	4a	44	15	4	—	—	—	13	1 – 7 (c)	—
	4b	23 – 1 (p)	14 – 1 (p)	7	2	1	7	4	2 (c) – 1 (p)	1 (c) – 1 (p)
	4c	5	1	—	—	—	—	—	—	—
DR6	4a	19	8	2	—	—	—	8	2 (c)	—
	4b	11	4	—	1	—	1	3	1 (c)	—
	4c	1	—	—	—	—	—	—	—	—
DR7	4a	10	2	1	—	—	—	1	1 (c)	—
	4b	11	6	6	4	2	4	2	3 (c) – 1	1 (t)
	4c	1	1	—	—	—	—	—	—	—
DR8	4a	42	20	4	—	—	—	19	3 (c) – 1 (t)	—
	4b	16 – 15 (p)	10 – 6 (p)	3	1	1	6 – 2 (p)	8 – 3 (p)	2 - 2 (c) – 1 (t)	3 (t) – 6 (p)
	4c	18	7	1	—	—	—	5	4 - 5 (t)	6 (t)

[a]The table lists the total number of samples and the number of thin sections made for each lithology in each dredge, as well as the number of thin sections in which each deformation event was identified. See text in Section 4 for details. p: polygenic breccia; t: talc-bearing veins; c: carbonate-bearing fractures.

may have been intruded into the footwall of the detachment fault and cooled from their magmatic temperature at any level in the axial lithosphere [*Cannat*, 1996], it is not possible to interpret their deformation styles and metamorphic facies in terms of depth with respect to geodynamically significant horizons such as the base of the brittle axial lithosphere, or the base of the hydrothermally altered domain. This motivated us to focus our study of deformation microstructures and of associated mineral assemblages on the ultramafic suite.

[23] The earliest deformation microstructures visible in ultramafic samples that have preserved some of their primary minerals are characterized by coarse grain sizes (0.5 to 1.5 mm for olivine relicts, and up to 2 mm for orthopyroxenes), with weak lattice preferred orientations (estimated with the optical microscope from the common extinction of a significant proportion of grains under polarized light) and occasional sub-grain boundaries in olivine. These microstructures are typical of plastic deformation in the low stress and high temperature conditions that prevail in the asthenospheric mantle (>1100°C [*Nicolas and Poirier*, 1976; *Poirier*, 1985]).

4.1. Plastic to Semi-brittle Deformation Type 1

[24] The earliest type of deformation that can be ascribed to the higher stress and lower temperature conditions of the mantle lithosphere is characterized by tight and weakly disoriented sub-grain boundaries and partial recrystallization of olivine (Figures 4a and 4b), and by recrystallization and local kinks of orthopyroxenes. Recrystallized grains range in size between 5 and 40 μm (with the smaller grain sizes in polymineral olivine and pyroxene assemblages) and do not appear to have a preferred crystallographic fabric. This episode of plastic (sub-grain boundaries and recrystallization) to semi-brittle (kinks) deformation is heterogeneously distributed at a millimeter scale, with olivine porphyroclasts free of sub-grain boundaries next to olivine with tight sub-grain boundaries. This deformation can only be identified in thin sections, and in samples that still contain olivine relicts (46 samples out of the 130 ultramafic samples in which thin sections were prepared). We observed this lithospheric plastic to semi-brittle deformation in only 2 samples from DR3, in 5 samples from DR7 and DR8, and in 1 sample from ROV DV 311 (DV311–19). Each of these 8 samples also contains amphibole and/or chlorite and therefore belongs to lithological type 4b (Table 3). By

contrast, olivine and orthopyroxene relicts in amphibole and chlorite-free serpentinized peridotites (lithological type 4a) have preserved asthenospheric-type microstructures (relicts of olivine were found in 24 type 4a samples; Table 3). There appears therefore to be a connection between the early episode of heterogeneous lithospheric plastic to semi-brittle deformation of the peridotite, and the presence of amphibole. This connection is emphasized by the observation of bands of fine-grained prismatic amphiboles with a shape preferred orientation parallel to the elongation of partly recrystallized olivine porphyroclasts (Figure 5a). Contacts between olivine and amphibole, however, are not clean as expected for equilibrium crystallization. Instead, recrystallized olivine grains near amphibole-rich bands appear
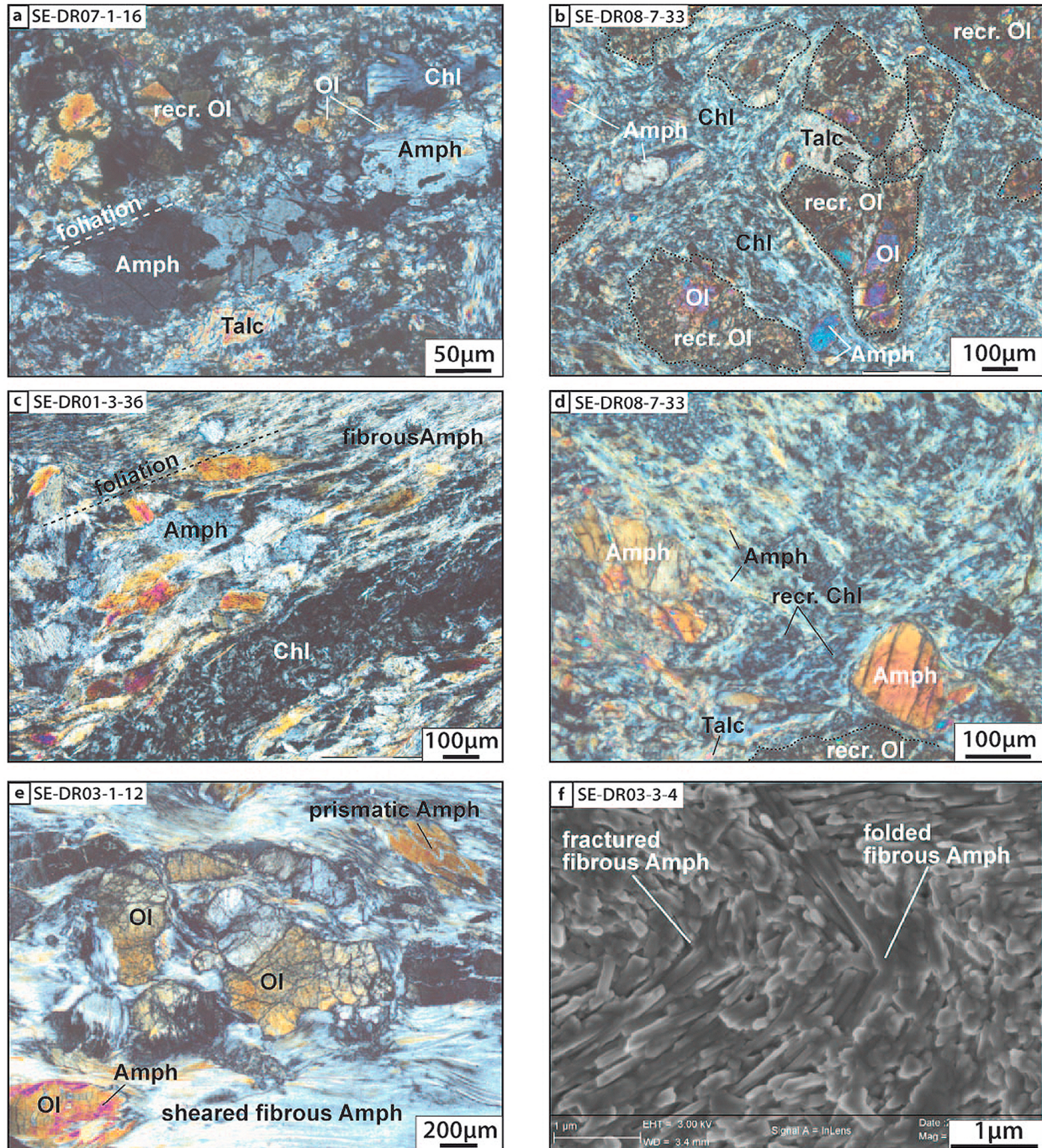

Figure 5

corroded. This suggests that amphibole crystallized at a later stage of plastic to semi-brittle deformation type 1.

4.2. Brittle Deformation Type 1

[25] Our observations in 4 out of the 8 thin sections that display plastic to semi-brittle deformation type 1 indicate that this deformation was overprinted by a brittle deformation, forming angular clasts of peridotite in a matrix comprised either of fibrous amphibole (in DR3; Figure 2d), or of amphibole, chlorite, and accessory zircon (in DR7 and DR8; Figure 5b). Many of the more extensively altered type 4b samples in DR1, DR3, DR7 and DR8 also contain angular clasts of a serpentine ± talc assemblage in an amphibole-bearing matrix (Figures 2b and 3b). These clasts probably also formed due to brittle deformation of the peridotite, prior to hydrothermal alteration. However, in Table 3, we only listed the 4 samples that unambiguously show this brittle failure overprint because the primary mineralogy of the peridotite is partially preserved. The relative chronology of the brittle deformation can be tightly constrained in these samples: it postdates the plastic to semi-brittle deformation of the primary peridotite mineralogy and it predates the crystallization of the amphibole-chlorite and zircon assemblages, or rather of their protolith.

4.3. Plastic to Semi-Brittle Deformation Type 2

[26] This deformation is again restricted to the amphibole and/or chlorite-bearing group of samples (lithological group 4b). It produces highly strained amphibole-bearing shear zones, up to 4cm-thick in our sample set (Figure 2e), and more pervasively if less intensely sheared samples (Figure 2f). We observed this second type of plastic to semi-brittle deformation in 31 of the 64 thin sections made for group 4b samples (Table 3). It appears to occur over a range of metamorphic conditions, characterized by a succession of deformed mineral assemblages. The earliest assemblage comprises prismatic amphibole oriented in the foliation and plagioclase in grains about 100 μm in size which are locally recrystallized into smaller grains (3 to 10 μm in size). In most samples, deformation of this early assemblage can only be inferred from the relationships between oriented prismatic amphibole and chlorite agregates which probably grew as a static replacement for plagioclase. The later and most common deformed assemblage comprises acicular to fibrous amphiboles (Figures 3e and 5c–5e). These are well-oriented and parallel to sub-parallel to the earlier prismatic amphibole foliation. In the most sheared samples, amphibole fibers are down to a few μm in length and underline tight folds and kinks indicative of a component of semi-brittle deformation (Figure 5f). In such highly sheared samples, the chlorite aggregates that developed as static replacement of plagioclase (Figure 5c), or as alteration coronae surrounding spinel from the host peridotite, are also deformed. Extensive plastic deformation of chlorite locally produces strong crystallographic preferred orientations (estimated with the optical microscope using a quarter wave plate) and finely recrystallized grains (<10 μm; Figure 5d).

[27] Our observations of samples affected by this second type of plastic to semi-brittle deformation indicate that it predated significant serpentinization, talc replacement and carbonatation: 1- prismatic to fibrous amphiboles grow next to corroded relicts of olivine (Figures 5a and 5e); 2- talc is either undeformed, or forms shear zones that are discordant and crosscut the amphibole-bearing

Figure 5. Photomicrographs of selected ultramafic samples. Sample number is shown in upper left. Polarized light except for SEM image in Figure 5f. Abbreviations: amphibole (Amph), chlorite (Chl), olivine (Ol). (a) Prismatic amphiboles form an elongated lens parallel to the trace of the foliation defined by recrystallized olivine in amphibole-bearing serpentinized peridotite (lith. type 4b; see sample in Figure 2f and less detailed photomicrograph in Figure 4b). Contacts between amphibole and olivine are mostly altered into undeformed fibrous amphibole and talc, with occasional chlorite. Locally, olivine fragments are enclosed in amphibole grains. (b) Clasts of partially recrystallized olivine in a sheared chlorite and amphibole-bearing matrix (lith. type 4b; see more detailed photomicrographs in Figures 5d and 6a). Fractures in some clasts are filled by talc. (c) Sheared amphibole-rich material in amphibole and chlorite-bearing serpentinized peridotite (lith. type 4b; see sample photograph in Figure 2b and less detailed photomicrograph in Figure 3b). Foliation is defined by oriented prismatic and fibrous amphibole. Chlorite forms elongated lenses and grows as a static replacement, probably of plagioclase. (d) Detail of sheared chlorite and amphibole matrix in amphibole and chlorite-bearing serpentinized peridotite (lith. type 4b; see less detailed photomicrograph in Figure 5b): well oriented amphibole fibers and recrystallized chlorite enclose porphyroclasts of prismatic amphibole. (e) Olivine porphyroclasts are enclosed and partially replaced by prismatic and fibrous amphibole in amphibole and chlorite-bearing serpentinized peridotite (lith. type 4b). (f) SEM image of amphibole-schist (lith. type 4b; see sample in Figure 2e and photomicrograph in Figure 3d). Individual amphibole fibers ≤5 μm in length outline folds and kinks.

foliation (Figure 6a); 3- amphibole-bearing shear zones are cut by serpentine veins that formed as arrays of extensional cracks, presumably associated with volume change during the serpentinization of the host ultramafic rocks (Figure 3f). Crosscutting serpentine veins, however, are commonly offset parallel to the amphibole and chlorite foliation, suggesting a late-kinematic opening. Crack-seal veins sub-parallel to the amphibole foliation in some amphibole-bearing shear zones (Figure 2d) also contain oblique serpentine fibers suggesting a component of shear during vein filling; and 4- Most carbonate and talc veins cut the amphibole shear zones at high angle. In a few samples where talc and carbonate veins parallel the
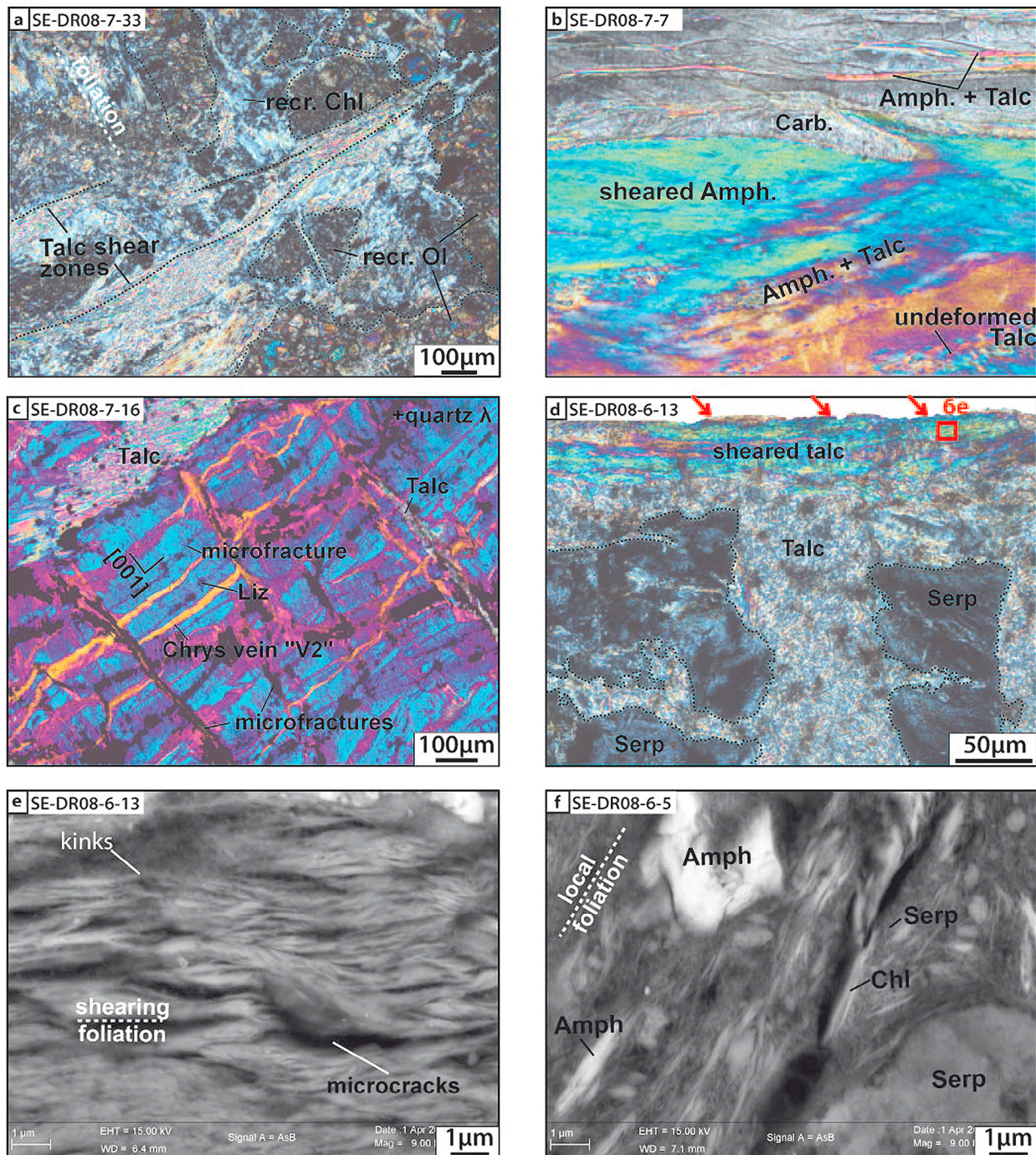

Figure 6

amphibole foliation (Figure 6b) SEM images show static growth of these minerals next to oriented amphibole fibers.

4.4. Serpentinization and Brittle Deformation Type 2

[28] Serpentinized ultramafic samples display classical mesh textures, commonly with nearly isotropic serpentine in the mesh cores, and outer rims of serpentine with a strong preferred orientation of the fast crystallographic axis parallel to the mesh bounding veins. A similar preferred orientation has been described in serpentinized peridotites of the Oman ophiolite and shown to correspond to pseudocolumnar lizardite, with the (001) planes parallel to the mesh bounding fractures [*Boudier et al.*, 2010]. In 68 out of 130 thin sections of ultramafic rocks (lithological types 4a, b and c; Table 3), we observed a preferred orientation and tight spacing (≤200 μm) of these mesh bounding fractures, resulting in a ribbon texture with a very strong serpentine preferred crystallographic fabric at thin section scale (Figure 6c). This ribbon texture is analogous to the "banded-growth" texture described by *Francis* [1956] and *Wicks* [1984]. It is common in samples from DR5 and DR6, and is present in most talc-bearing samples from DR1 and DR8 (Table 3). In many samples, it is cut by later sub-parallel extensional veins of serpentine (Figure 6c), equivalent to the "V2" veins described by *Dilek et al.* [1997] and *Andreani et al.* [2007].

[29] Many samples that have this ribbon serpentine texture also present arrays of discordant serpentine or talc-filled cracks and veins (Figure 6c). In 5 samples, we also observed limited undulose extinction of the serpentine meshwork within 0.5 mm of some of these fractures, but in most samples, the serpentinite forms angular clasts with no internal deformation (Figure 4d). In samples that are extensively altered into talc, we also observed that the ribbon-shaped serpentine mesh was preferentially altered into talc, while serpentine in the later "V2" extensional veins was better preserved. The talc veins are up to 1 mm-wide, some contain angular clasts of the host serpentinite (Figure 4d). Talc grows statically either as a replacement of these serpentine clasts, or as short fibers perpendicular to the veins margins, forming 5 to 10 μm-thick crack-seal bands (Figure 4d). This latter texture suggests that brittle deformation of the serpentinite into angular clasts was accompanied by significant fluid input, allowing for the progressive opening and filling of the talc-bearing veins.

[30] A few ultramafic samples from DR5, DR6 and DR8 display arrays of angular carbonate-filled fractures, up to 100 μm-thick, that also formed during limited brittle deformation of the serpentine mesh and are therefore also ascribed to brittle deformation type 2. These crack commonly re-use pre-existing serpentine veins and are spaced by ≥100 to 500 μm.

4.5. Plastic to Semi-Brittle Deformation Type 3

[31] Talc growth in the ultramafic samples follows on the brittle failure of the serpentine meshwork and is mostly static. However, most talc-bearing

Figure 6. Photomicrographs of selected ultramafic samples. Sample number is shown in upper left. Polarized light except for SEM images in Figures 6e and 6f. Polarized light with a quater wave plate added in Figure 6c. Abbreviations: amphibole (Amph), chlorite (Chl), serpentine (Serp), carbonate (Carb). (a) Talc-bearing microshear zones in amphibole and chlorite-bearing serpentinized peridotite (lith. type 4b; see other photomicrographs of this sample in Figures 5b and 5d). Talc-bearing shear zones cut across earlier amphibole and chlorite-bearing microshears, which define a crude foliation. (b) Detail of carbonate veins in amphibole and chlorite-bearing serpentinized peridotite (lith. type 4b). Undeformed carbonate forms lenticular veins in sheared fibrous amphibole. Talc grows as a static replacement of amphibole. (c) Ribbon serpentine in talc-bearing serpentinized peridotite (lith. type 4c). Ribbons are made of columnar lizardite with their [001] slow crystallographic axis oriented sub-perpendicular to a set of sub-parallel micro-fractures. This produces a strong crystallographic preferred orientation at thin section scale (visible in blue with the adjunction of a quarter wave plate). Later chrysotile extensional veins show in yellow due to the preferred orientation of the chrysotile fibers in the veins opening direction. A set of sub-orthogonal microfractures are preferentially altered into talc. (d) Micro-shear zone in talc-bearing serpentinized peridotite (lith. type 4c; see sample in Figure 2g and SEM image in Figure 6e). Angular clasts of serpentinized peridotite are partially replaced by talc. Shear zone is 20 to 100 μm-thick and made of talc with a strong crystallographic preferred orientation. (e) SEM image of talc micro-shear zone in talc-bearing serpentinized peridotite (lith. type 4c; see sample in Figure 2g and photomicrograph in Figure 6d). Talc plates ~1 μm in size are strongly oriented and locally fractured. Microcracks are also observed suggesting a component of dilatant brittle deformation. (f) SEM image of sheared matrix in polygenic breccia with clasts of serpentinized peridotite and of a chlorite-rich metagabbroic material (lith. type 4b; see sample in Figure 2h and photomicrograph in Figure 4c). Amphibole occurs as porphyroclasts and as fractured fibers which we infer were mechanically rotated into the local foliation, underlined by very small (≤1 μm) chlorite and serpentine fibers.

samples also show heterogeneously distributed arrays of 10 to 200 μm-thick shear zones (Figures 6a and 6d). SEM images reveal that talc in these shear zones forms well oriented plates, 1 μm to 5 μm in size (Figure 6e). Some of these plates are kinked or fractured, and microcracks are observed sub-parallel to the foliation. This is consistent with a combination of plastic and dilatant brittle deformation mechanisms (Plastic to semi-brittle deformation type 3), as observed in talc deformation experiments [*Escartín et al.*, 2008b]. These talc shear zones are thin, but common and most are continuous across a given thin section. We thus infer that this 3rd event of plastic deformation may have accommodated a significant strain.

[32] Carbonate is a common vein mineral in samples from DR5, DR6 and DR8. It is undeformed, except in one sample (DR8-6-16) where we observed a sheared 50 μm-thick carbonate vein, which we also ascribe to plastic to semi-brittle deformation type 3 because it offsets the serpentine meshwork.

4.6. The Formation of Polygenic Tectonic Breccia in DR3 and DR8

[33] Amphibole-bearing ultramafic breccias collected in DR8 above the Logatchev vent site (Figure 2h) contain centimeter-sized angular to rounded clasts of amphibole and talc-bearing serpentinite, of serpentinite, and of metagabbro. Some clasts of amphibole and talc-bearing serpentinite contain a preexisting foliation defined by prismatic and acicular amphibole and typical of plastic to semi-brittle deformation type 2. These samples were first interpreted as sedimentary. However, this interpretation was revised during onshore studies because the matrix of these breccias is made of smaller angular clasts of serpentine and amphibole (Figure 6f) in a fine-grained matrix made of serpentine and chlorite. This matrix contains anastomosing shear zones up to 200 μm-thick with a strong crystallographic preferred orientation of serpentine and chlorite fibers (Figure 4c). Talc replacing serpentine next to amphibole-rich clasts is also locally sheared. These breccias are therefore reinterpreted as tectonic in origin. Because some clasts display amphibole foliations typical of plastic to semi-brittle deformation 2 and because angular clasts of serpentinite indicate that brecciation postdated serpentinization, we tentatively propose that brittle failure leading to the formation of the breccias may be equivalent to the brittle deformation type 2 and that the subsequent plastic to semi-brittle

deformation of the breccia matrix may be equivalent to plastic deformation type 3 in the other ultramafic samples (Table 3).

[34] We recovered only one sample of a similar matrix-supported breccia in the Ashadze region (Figure 3e). Compared to the polygenic breccia in DR8, this sample does not include clasts of amphibole-bearing serpentinized peridotite. It also displays evidence for a later stage of cataclastic deformation, forming clasts of clasts in a matrix made primarily of crushed chlorite and serpentine in serpentine-rich parts of the sample (Figure 3e), and of crushed chlorite and epidote in serpentine-poor parts of the sample.

5. Primary and Secondary Mineral Compositions in Deformed and Undeformed Ultramafic and Gabbroic Samples

[35] The amphibole-bearing ultramafic samples represent between 3.4 and 31.2% in volume of our dredges (Table 2) and have played a key role to accommodate deformation prior to the onset of serpentinization (Table 3). Our objective is first to provide mineral chemistry constraints as to the nature of their protolith. For this we have analyzed: 1- the composition of olivine and spinel relicts of the primary peridotite assemblage in selected amphibole-bearing ultramafic samples (Figures 7a and 7b); 2- the composition of the earliest generations of amphiboles, of accessory zircon and of plagioclase when present in these selected samples (Figures 7c, 7d, and 8); and 3- the composition of the earliest generations of amphiboles and of plagioclase and zircon when present in a selection of evolved gabbroic samples for comparison (Figures 7c, 7d, and 8). Our second objective is to provide constraints on the metamorphic conditions that prevailed during deformation (Figure 9). For this we present microprobe data for deformed mineral assemblages associated with the plastic to semi-brittle deformation types identified in the ultramafic samples.

[36] Microprobe analyses were performed on the CAMPARIS Cameca SX50 electron microprobe, with a 5 μm beam, a 15 kV tension and 40 nA beam current. Counting times on peaks were 5 to 10s. With these conditions, we obtained reproducible Hf, Zr, P, and Y concentrations in zircons. Table S4 shows selected analyses. The full set of microprobe data used in Figures 7–9 is accessible in the Petrological Database of the Ocean Floor (PetDB).
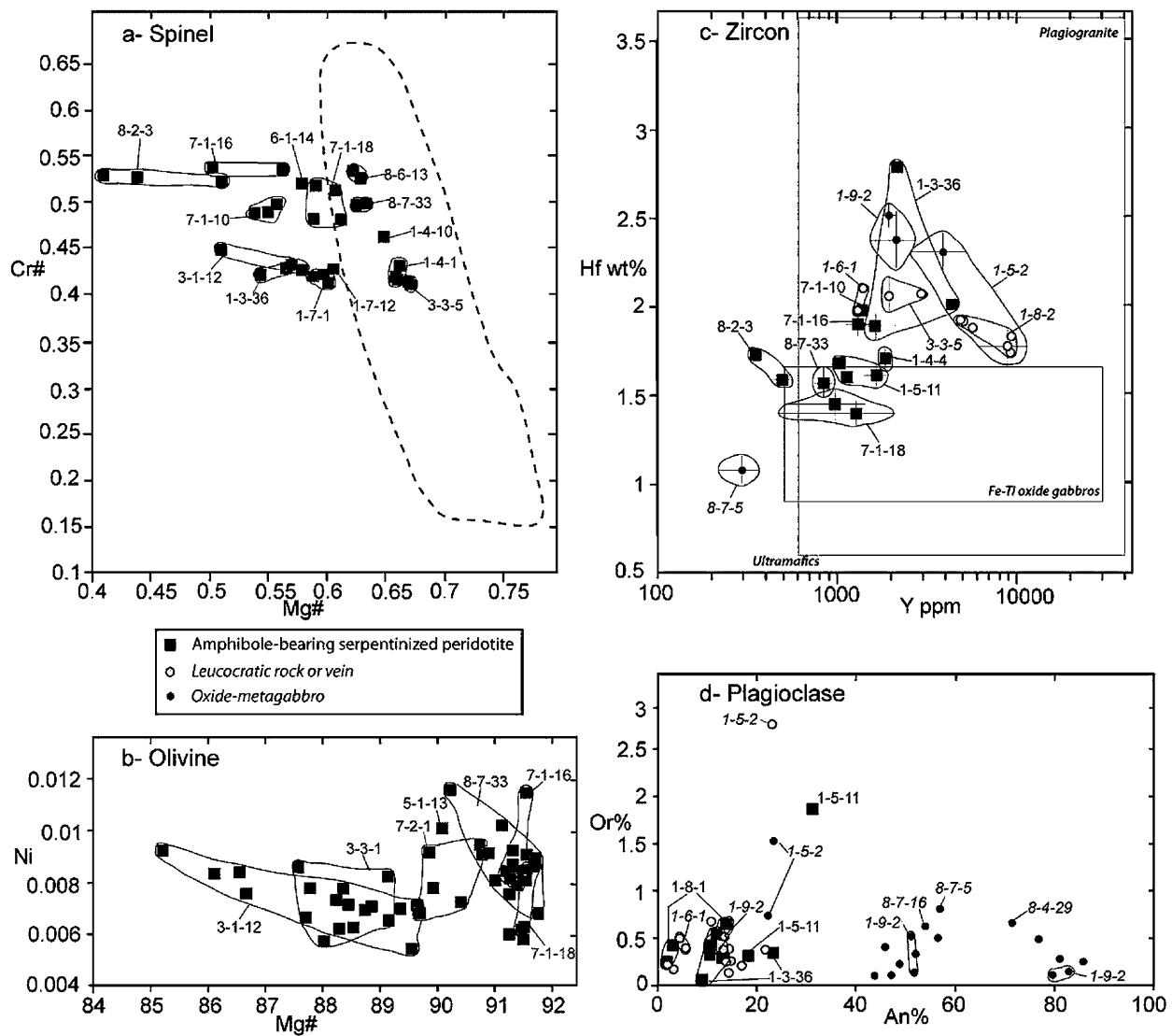
Figure 7. Microprobe composition of spinel, olivine, zircon and plagioclase compositions measured in amphibole and chlorite-bearing ultramafic samples (lith. type 4b). Zircon and plagioclase compositions in selected metagabbroic samples are plotted for comparison. Sample numbers are shown. Each point represents the composition of one crystal. Fine lines circle data points for individual crystals in each analyzed samples. (a) Cr# versus Mg/(Mg + Fe + Mn) in the cores of spinel relicts. The trend for MAR abyssal peridotites (dashed line) is drawn from *Ghose et al.* [1996] and *Cannat and Casey* [1995]. Spinels in lithological type 4b samples tend to depart from this trend toward more iron-rich compositions. Samples from the Ashadze (DR1, DR3 and DR5) and Logatchev (DR6, DR7 and DR8) regions show distinct Cr# values, consistent with a lesser overall degree of mantle partial melting in the Ashadze region [*Silantyev et al.*, 2011]. (b) Ni vs Forsterite content in the cores of olivine relicts. Typical abyssal peridotites have Fo% between 90 and 92. Olivine in lithological type 4b samples tends to depart from this trend toward more iron-rich compositions. Spread of Ni values is artifact of short microprobe counting times. (c) Hf versus Y in zircons. Error bars show standard deviation for grains in which more than one measurement was made. Grey rectangles outline the compositional domains identified by *Grimes et al.* [2009] for ultramafic rocks, oxide gabbros and plagiogranites from various abyssal locations. (d) Orthoclase vs anorthite content in plagioclase. Due to extensive alteration, plagioclase was preserved in only a few lithological type 4b samples, all of them in DR1. It is compositionally similar to plagioclase from the most leucocratic gabbroic samples.
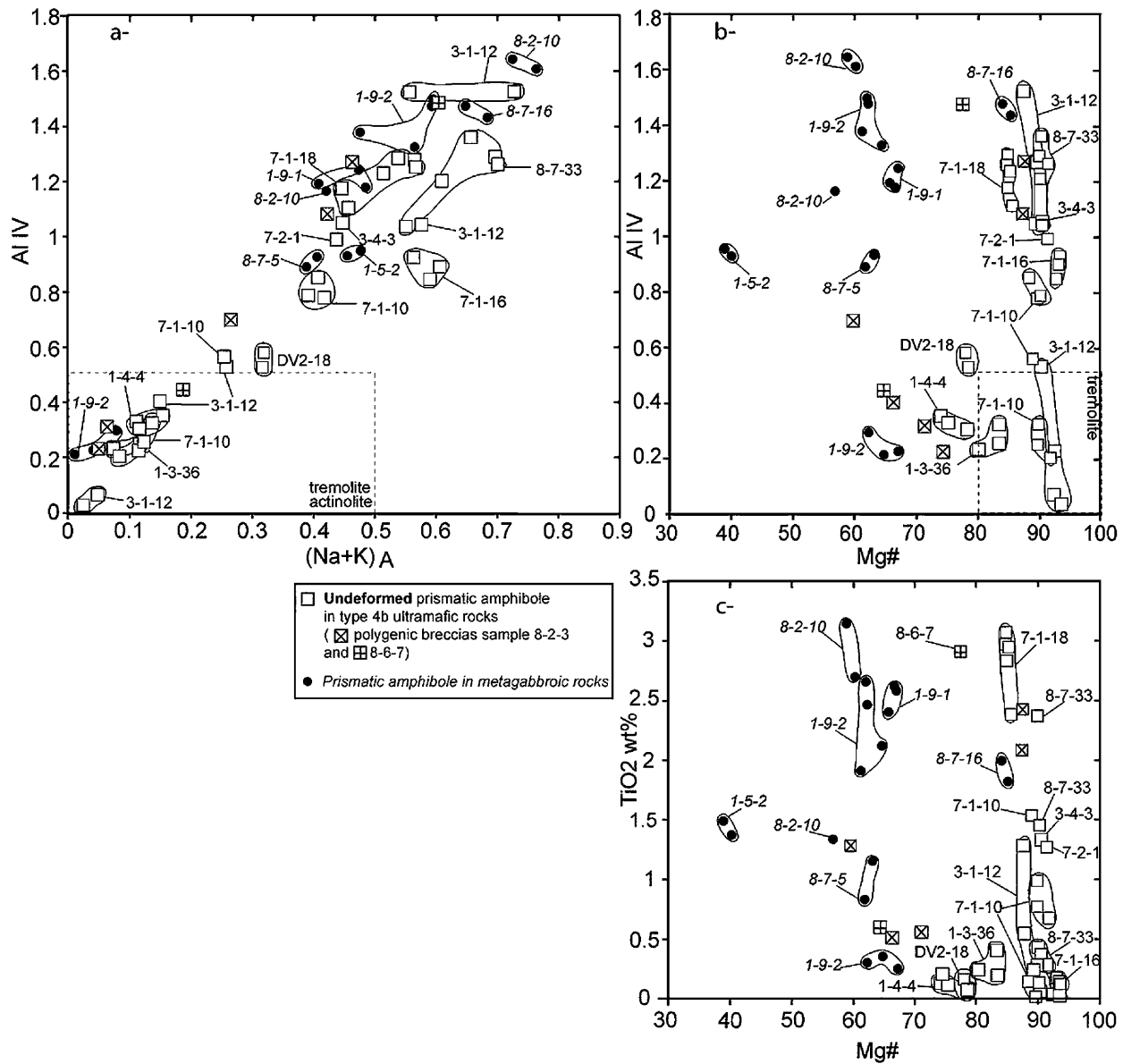
Figure 8. Microprobe composition of undeformed prismatic amphibole in amphibole and chlorite-bearing ultramafic samples (lith. type 4b) and in selected metagabbroic samples. Sample numbers are shown. Each point represents the composition of one crystal. Fine lines circle data points for individual crystals in each analyzed samples. (a) Al^{IV} versus $(Na^+K)_A$. Measured compositions span the pargasitic trend, from high Al^{IV} and $(Na^+K)_A$ pargasitic compositions, through hornblende, to low Al^{IV} and $(Na^+K)_A$ tremolites. (b) Al^{IV} versus Mg# and (c) TiO_2 (wt%) versus Mg#. Two trends are visible: an iron-rich trend at Mg# 60–70 corresponds to metagabbroic samples, and to amphiboles in polygenic ultramafic breccias, and an iron-poor trend at Mg# 85–95 corresponds to most lithological type 4b samples. Tremolitic amphiboles from DR1 type 4b samples plot between these two trends. Sample 8-7-16 is cm-thick oxide-bearing metagabbronorite in serpentinized peridotite. We propose that low iron in prismatic amphiboles in the ultramafic samples results from Fe-Mg exchange between an evolved gabbroic melt and the minerals of the host peridotite (see olivine and spinel trends in Figures 7a and 7b).

5.1. Mineral Compositions in the Amphibole-Bearing Ultramafic Samples and in Selected Gabbro Samples

[37] Olivine and spinel compositions in amphibole-bearing ultramafic samples range from typical of residual abyssal peridotites (olivine Fo contents between 90 and 92% and spinel Cr# between 35 and 55) to iron-enriched compositions with Mg# values as low as 85 in olivine and 40.8 in spinel (Figures 7a and 7b). In sample DR3-1-12, that contains both
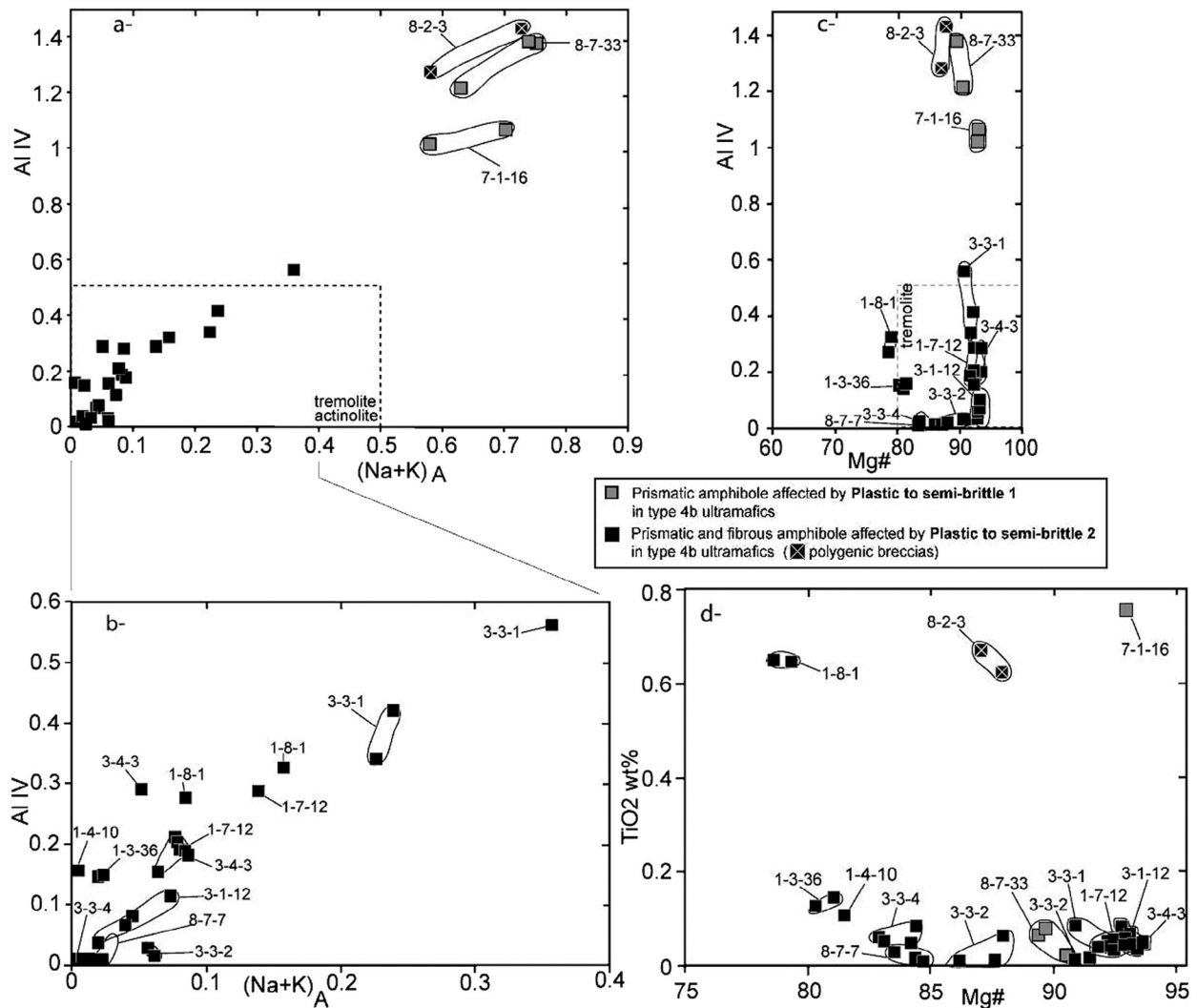
Figure 9. Microprobe composition of deformed prismatic and fibrous amphibole in amphibole and chlorite-bearing ultramafic samples (lith. type 4b). Sample numbers are shown. Each point represents the composition of one crystal. Fine lines circle data points for individual crystals in each analyzed samples. (a) Al^{IV} versus $(Na^+K)_A$. Amphiboles affected by plastic to semi-brittle deformation type 1 are pargasites or hornblende; amphiboles affected by plastic to semi-brittle deformation type 2 are tremolites. (b) Detail of Figure 9a. (c) Al^{IV} versus Mg#. (d) TiO_2 (wt%) versus Mg#. Most deformed amphiboles have Mg# > 90. A few samples from DR1, DR3 and DR8, however, have more iron-rich amphiboles (Mg# 80–90), intermediate in composition to amphiboles in metagabbroic samples (Figure 8).

olivine and spinel, these minerals show a wide range of iron content (Figures 7a and 7b). Polygenic breccia sample DR8-2-3 contains the most iron-rich spinels but no relict olivine (Figure 7a).

[38] Prismatic amphiboles in most samples from DR7 and DR8 (Logatchev area) are titanium-rich hornblendes with Mg# between 83.5 and 93.3 (Figure 8). In the polygenic breccia sample DR8-2-3, that contains the most iron-rich spinels, there are two types of prismatic amphiboles: Ti-rich, Mg# 87 hornblendes are found in clasts of amphibole-bearing serpentinite, and Al-poor

tremolitic-hornblendes and tremolites, with moderate to low TiO2 contents (<1.3wt%) and low Mg# (60 to 87) are found in the more finely brecciated chlorite and serpentine material (Figure 8). These iron-rich amphiboles are similar in composition to those in an oxide-gabbro dikelet in sample DR8-7-5 (Figure 8), while the Ti-rich hornblendes in the clasts are similar to brown prismatic amphibole in a metagabbro gabbro vein from serpentinized peridotite sample DR8-7-16, which contains An 54 plagioclase (Figure 7d) and poikilitic phlogopite (Table S4). The most common metagabbroic rocks in DR7 and DR8 are fine-grained and partly

recrystallized oxide-metagabbros with An 52 to 57 plagioclase neoblasts, and Ti-rich, Mg# 56 to 69 hornblende (DR8-2-10; Figures 7d and 8).

[39] Prismatic amphiboles in amphibole-bearing serpentinized peridotites from DR3 (Ashadze region) grow in and around olivine relicts and are Al-poor hornblendes and tremolites, with moderate to low Ti content and Mg# between 87.5 and 94 (Figure 8). In sample DR3-1-12, Al-rich and Ti-poor hornblende is also present as porphyroclasts in sheared fibrous amphiboles (Figure 5e). In amphibole-bearing ultramafic samples from DR1 (Ashadze region), prismatic amphiboles are tremolitic, with Mg# between 72 and 82 (Figure 8). Prismatic tremolites similar in composition except for lower Mg# (61.25 to 79.65) are found in leucocratic injections in the oxide-gabbro sample DR1-9-2 (Figures 2a, 3a, and 8).

[40] Plagioclase relicts in amphibole-bearing ultramafic samples are rare and extensively altered. When present (Figure 3b), plagioclase has a low anorthite content (~An 25; Figure 7d) comparable to that of plagioclase from leucocratic injections in the gabbroic samples (Figure 7). Zircon is present in the amphibole-rich portions of most type 4b ultramafic samples (Figure 4a). It has hafnium concentrations between 1.4 and 2.8 wt% and yttrium concentration between 350 and 4435 ppm (Figure 7c). Zircon in Ti-hornblende-bearing ultramafic samples from DR7 and DR8 plots in the lower Hf and Y range, while zircon from tremolite-bearing DR1 samples plots in the higher Hf and Y range, near zircon from the most evolved oxide-gabbros and from leucocratic injections. We did not find zircon in thin sections of amphibole-bearing samples from DR3. Zircon grains from altered oxide-gabbros and leucocratic injections in the metagabbros (Figure 3a) have similar Hf and Y contents (Figure 7c), consistent with the field of zircons from mid-ocean ridge oxide-gabbros and plagiogranites, based on the study of *Grimes et al.* [2009].

5.2. Mineral Assemblages Associated With the Plastic to Semi-Brittle Deformation Types in the Ultramafic Rocks

[41] Plastic to semi-brittle deformation type 1 (Table 3) involves partial recrystallization of the primary mineralogy of the peridotite (olivine and pyroxenes). In some samples, we also observed prismatic amphibole elongated parallel to the olivine-pyroxene foliation (Figure 5a). Olivine porphyroclasts and neoblasts have similar compositions, typical of residual abyssal peridotites (Fo% 91–91.7), or enriched in iron (Fo% 85.2–89.6). Oriented

prismatic amphiboles are magnesian-rich hornblendes, comparable in composition to the prismatic amphiboles found as porphyroclasts in chlorite-rich regions of the same samples (Figure 5d), except for a lower Ti content (Figure 9).

[42] Plastic to semi-brittle deformation type 2 is characterized by deformation of prismatic to fibrous amphibole, with chlorite lenses that are mostly undeformed (Figure 5c). Chlorite shear zones are found only in amphibole-poor domains (Figure 5d and Table S4). Prismatic amphiboles oriented in the foliation are tremolitic in composition, with $TiO_2 < 0.65\%$ (Figure 9). Locally, they show incipient recrystallization together with plagioclase with low An contents: 3 to 13. Fibrous amphiboles in shear zones (Figures 3d, 5c, 5e, and 6b) are also tremolites, with up to 0.7% TiO_2 (Figure 9). In samples from DR3, these fibrous amphiboles have slightly higher Al_2O_3 and Na^+K contents, but similar iron content than the undeformed prismatic amphiboles that are locally seen to grow in olivine relicts (Figure 5e). We note that fibrous secondary amphiboles in the other analyzed ultramafic samples tend to have higher Mg# than the earlier prismatic amphiboles in the same sample: in DR1 we measured Mg# of 74 to 83 for prismatic amphiboles and of 80 to 93 for fibrous amphiboles and in DR7 and DR8 we measured Mg# of 84.7 to 91.7 for prismatic amphiboles and of 83.5 to 94 for fibrous amphiboles (Figures 8 and 9).

[43] Finally, plastic to semi-brittle deformation type 3 is associated with the growth of oriented talc in shear zones in serpentinized peridotite samples, and of oriented fibers of serpentine, chlorite and occasional talc in sheared matrix of polygenic breccia samples (Figures 3e, 4c, and 6f). Representative compositions for talc and chlorite are listed in Table S4.

6. Discussion

6.1. Gabbroic Injections in Peridotites as Protolith of the Amphibole-Bearing Serpentinized Peridotites

[44] Amphibole-bearing ultramafic samples contain both olivine and spinel relicts with compositions typical of residual peridotites (except for lower Mg# in some olivine and spinel relicts; Figures 7a and 7b), and amphibole, plagioclase and zircon with compositions similar, (except for higher Mg# in amphiboles) to those of minerals in gabbroic samples (Figure 8). This suggests, as proposed by *Jöns et al.* [2009] for drilled samples from Holes 1270A,

1270C and 1270D (ODP Leg 209; Figure 1), that the protolith for these rocks was a mixture of residual peridotite and evolved gabbroic rocks. This interpretation is consistent with our textural observations: amphibole-rich veins and infiltrations are observed in the ultramafic rocks and there are angular clasts of variably altered peridotite in the amphibole-rich material (Figures 2b and 5e). The local iron enrichment observed in the olivine and spinel of our amphibole-rich samples (Figures 7a and 7b) can be explained by a reaction of the peridotite host rock with a percolating evolved gabbroic melt. Similar chemical trends have been described in ultramafic samples from the 15°N and Kane areas [*Cannat and Casey*, 1995; *Cannat et al.*, 1997].

[45] The primary composition of the gabbroic component injected in the peridotites is difficult to decipher due to extensive hydrothermal alteration. Plagioclase has been altered into chlorite except in some samples from DR1 and we have not observed relicts of pyroxenes which could have been part of the primary magmatic assemblage. Zircon Hf-Y contents span the range of compositions measured by *Grimes et al.* [2009] in abyssal oxide-gabbros and plagiogranites. Titanium-rich amphiboles are found mostly in samples from DR7 and DR8 (Figure 8), which also contain zircon with lower Hf and Y contents (Figure 7c). By contrast, amphiboles in DR1 ultramafic samples are titanium-poor, and the anorthite content of plagioclase (An 2–30) is similar to values measured in leucocratic injections in the metagabbroic suite of the same dredge (Figure 7d). This suggests that the injected melts may have been more leucocratic in DR1, and closer in composition to the parent melts of the oxide-bearing metagabbros in DR7 and DR8.

[46] Amphibole-bearing ultramafic lithologies are present in all the dredges considered in this study (Table 2). They are, however more abundant in DR1, below the old corrugated surface in the Ashadze region (Figure 1c). Compositionally, the amphiboles in ultramafic samples from DR1 also tend to have higher iron contents (Mg# 80–90), than amphiboles in ultramafic samples from the other dredges (Mg# 85–95; Figure 8). We propose that this difference could be due to the fact that residual peridotites in DR1 interacted with a larger relative volume of evolved gabbroic melts so that the iron-magnesium content of this intruding melt was less modified by interaction with the peridotite host. Amphibole-bearing serpentinized peridotites are less abundant in DR3 and DR5 that also contain less metagabbros (Table 2). Our interpretation of this link between the abundance of gabbroic

samples, and of amphibole-bearing serpentinized peridotites in a given dredge, is that the injection of evolved gabbroic melts in the residual ultramafic rocks occurs preferentially next to larger differentiating gabbroic bodies. Similar evolved melts have been proposed to have formed by hydrous remelting of gabbros following the introduction of hydrothermally derived fluids [*Koepke*, 2005; *Koepke et al.*, 2007]. This would be consistent with the highly hydrous composition of the inferred primary gabbroic mineralogy in most of our samples, which appears to have been mostly comprised prismatic amphibole, plagioclase and accessory zircon. The involvement of hydrothermal fluids in the magmatic fractionation process is, however, not supported by zircon oxygen isotopes compositions reported by *Grimes et al.* [2011] for evolved gabbroic rocks drilled at ODP site 1270.

[47] Amphibole-bearing ultramafic rocks similar to those described here have been reported from most Mid-Atlantic ridge ultramafic exposures [*Escartín et al.*, 2003; *Dick et al.*, 2008; *Boschi et al.*, 2006a; *Cannat et al.*, 1992; *Cannat and Casey*, 1995; *Cannat et al.*, 1997; *Petersen et al.*, 2009; *Schroeder and John*, 2004; *Schroeder et al.*, 2007] and therefore appear as a characteristic lithological component of the footwall next to MAR detachments. *Escartín et al.* [2003] who worked on extensively altered and deformed talc-chlorite and amphibole schists cored in a corrugated fault zone at 15°45′N, have proposed that these rocks formed from a peridotite protolith due to Ca-Si-Fe-Al hydrothermal metasomatism. Other authors working on variably altered and strained samples, have proposed, as we do here, a gabbroic protolith for these amphibole-bearing ultramafic lithologies [*Cannat et al.*, 1992, 1997; *Cannat and Casey*, 1995; *Jöns et al.*, 2009; *Schroeder and John*, 2004; *McCaig et al.*, 2007; *Boschi et al.*, 2006b].

[48] The tectonic context of the proposed gabbroic injections can be refined based on the microstructural characteristics of relict olivine in the amphibole-bearing ultramafic samples. Out of 59 thin sections made in this rock type, only 19 still contain relict olivine, and out of these 19, 8 display the heterogeneous recrystallization and kinking characteristic of plastic to semi-brittle deformation type 1, which we interpreted (Section 4) as a relatively high stress deformation in the axial lithosphere. By contrast, we have observed that relict olivine in amphibole-free ultramafic samples display the coarse grain sizes and occasional sub-grain boundaries typical of the low stress-high temperature deformation conditions that prevail in the asthenospheric mantle

[*Nicolas and Poirier*, 1976; *Poirier*, 1985]. This leads us to propose that gabbroic injections leading to the formation of the amphibole-bearing serpentinized peridotites occurred preferentially in peridotites that had been subjected to plastic to semi-brittle deformation type 1.

[49] Interpreted in the context of an axial denudation system, this would suggest that melts preferentially infiltrated domains of the footwall that had been sheared while still in the plastic to semi-brittle part of the lithosphere. A further constraint on the context of these magmatic injections is that the peridotite component of amphibole-bearing serpentinized peridotites occurs as clasts (Figures 2b and 5b). In samples that still contain fresh olivine, we have shown that these clasts formed during brittle deformation type 1 (Section 4). This leads us to propose that the gabbroic melts were injected into the peridotite as it entered the brittle part of the axial lithosphere. In the conceptual sketch of Figure 10, we also tentatively root the detachment in plastic to semi-brittle deformation type 1 shear zones and propose that the injection of evolved melt preferentially occurred in the domains closest to the fault.

6.2. Strain Localization in Hydrothermally Altered Gabbroic Injections

[50] Nearly half of the thin sections made in amphibole-bearing serpentinized peridotites display moderate to strong plastic to semi-brittle deformation of a tremolite ± chlorite assemblage, which we infer grew as a hydrothermal replacement of the gabbroic material, or of the peridotite + gabbro mixture. The highest strains are observed in tremolite-rich shear zones, in which relicts of residual olivine are surrounded by tremolite (Figure 5e). This, and the observation of serpentine veins crosscutting tremolite-bearing shear zones (Figure 3f), indicate that the tremolite shearing event predated the bulk serpentinization of the peridotites. This deformation event spans downgrade metamorphic conditions from the field of stability of plagioclase, which recrystallizes with tremolite in some samples, to the field of chlorite stability, which subsequently replaces plagioclase (Section 4). The lack of serpentine in this deformed assemblage and the presence of relict olivine suggest temperatures still in excess of $400°C$ [*O'Hanley*, 1996] for the end of this second plastic to semi-brittle deformation event, while the stability of tremolitic amphibole indicates maximum temperatures $<800°C$ [*Boyd*, 1959].

[51] Plastic to semi-brittle deformation type 2 is found in every dredge (Table 3), from DR1 beneath the old corrugated surface at Ashadze, to DR7 and DR8 next to the Logatchev vents. The deformation conditions described for our samples are also similar to those proposed by *Jöns et al.* [2009] for a set of sheared amphibole-bearing serpentinized peridotites drilled at IODP Site 1270 (Figure 1), in an off-axis corrugated surface [*Garcés and Gee*, 2007]. Similar tremolite-bearing schists have also been sampled repeatedly in exhumed ultramafic terranes next to the Mid-Atlantic Ridge: at the 15°45′N off-axis core-complex studied by *Escartín et al.* [2003], in the 23°30′N Kane Megamullion core complexes studied by *Dick et al.* [2008], and next to the ultramafic-hosted Lost City vents at 30°N [*Boschi et al.*, 2006a; *Schroeder and John*, 2004]. These tremolite-bearing schists therefore appear to form quite systematically in ridge axis peridotite denudation systems. The timing of formation of these schists with respect to serpentinization of the ultramafics was discussed in these earlier studies and *Jöns et al.* [2009] develop petrological arguments that support our interpretation of these tremolite schists as being for the most part pre-serpentinization.

[52] In the conceptual sketch of Figure 10, we propose that tremolite-bearing shear zones localize deformation at temperatures between $\sim750°$ and $400°C$. The spatial extent of this $750°$ to $400°C$ temperature domain in the detachment footwall is expected to be controlled primarily by hydrothermal fluxes. High fluxes will cool the rock quickly and buffer it to the fluid's temperature. In places where the detachment fault zone and its upper footwall channel hot ($\sim400°C$) hydrothermal fluids [e.g., *McCaig et al.*, 2007], the lower temperature portion of this tremolite deformation domain may thus have a large spatial extent, and accommodate large cumulated strains. By contrast, in places where the detachment and its footwall channel cooler hydrothermal fluids, this tremolite deformation domain may be small. Similarly, the greenschist facies temperature conditions that prevailed in our deformed samples during and after serpentinization may have been maintained over a large depth-range in regions of the detachment fault and footwall that were swept by warm ($\sim200°$- 350°C) hydrothermal fluids. In general, spatial and temporal changes in the hydrothermal circulation at a given fault or footwall location should lead to large spatial and time variability in the distribution of the deformation types sketched in Figure 10.
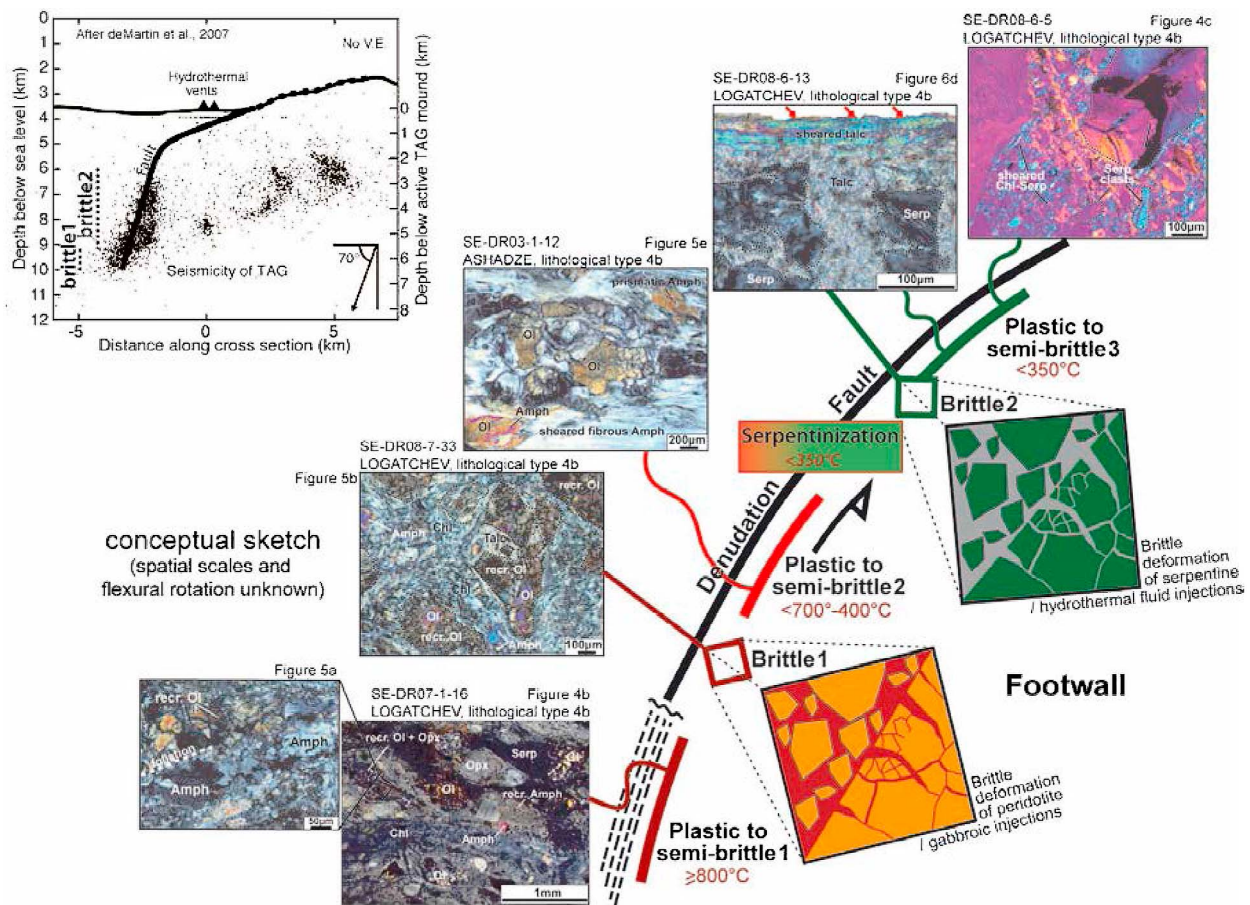
Figure 10. Conceptual sketch of the sequence of plastic and brittle deformation in ultramafic rocks in the upper 500m of the footwall at a MAR detachment fault, based on our microstructural and petrological observations. Selected photomicrographs from Figures 5 and 6 illustrate these deformations. The sequence includes two brittle deformations, both associated with fluid injection (magmatic or hydrothermal), and three plastic to semi-brittle deformations. A sampling bias may have prevented recovery of the least cohesive lithologies, such as gouges that may also accommodate large strain in the fault and footwall and are not represented here. Brittle deformations affect either fresh peridotite (brittle deformation 1), or already serpentinized peridotite (brittle 2) and are associated in both cases with fluid injection: an evolved gabbroic melt for brittle deformation 1, and a Si-rich hydrothermal fluid for brittle deformation 2. Brittle deformation types 1 and 2 may be associated with the sustained microseismicity observed at detachment fault settings of the Mid-Atlantic Ridge, as suggested in the inset which is drawn from *deMartin et al.* [2007]. Plastic to brittle-plastic deformation 1 is mostly anhydrous, with dynamic recrystallization of olivine and pyroxenes at temperatures probably >800°C. Plastic to brittle-plastic deformation 2 is restricted to amphibole and chlorite-bearing ultramafic samples and controlled by deformation and syn-tectonic crystallization of tremolite at temperatures above the upper stability of serpentine (400°C). Finally, plastic to brittle-plastic deformation 3 is accommodated by thin talc, or chlorite+serpentine ± talc shear zones and corresponds to greenschists facies temperature conditions. The sketch is not drawn to scale: we expect that the distribution, in space and time, of each deformation type should be controlled both by the abundance of gabbroic injections at depth near the base of the brittle axial lithosphere, and by the pattern of hot and cold hydrothermal plumes and sinks in the permeable domain in the fault and in the footwall.

6.3. Serpentinization and Talc Crystallization

[53] Constraining the location and timing of pervasive serpentinization in the footwall of axial detachments is an important objective. Our observations show that pervasive serpentinization post-dates the plastic to semi-brittle deformation of

tremolite-bearing samples in all studied dredges. It produces serpentinites with two types of textures: equant-mesh or ribbon (Figure 6c). The ribbon serpentine texture is observed in many samples from all dredges (but DR1 in which serpentine textures are obscured due to extensive replacement by talc). Ribbon textures are also reported by *Boschi*

et al. [2006a] in serpentinites from the Atlantis Massif (30°N MAR). As proposed by *Wicks* [1984], we infer that ribbon textures in serpentinites result from a strong preferred orientation of cracks which formed in the unserpentinized material and subsequently controlled the penetration of the serpentinizing fluid. This pre-serpentinization cracking event appears widespread in our samples.

[54] Talc crystallization in our samples occurs in two ways. In amphibole and/or chlorite-bearing ultramafic samples (lithological type 4b) talc crystallized in the rims of ultramafic clasts, next to the amphibole and chlorite-rich domains (Figures 3b and 4a). These talc rims postdate plastic to semi-brittle deformation type 2: undeformed talc is common next to sheared tremolite and chlorite. In amphibole and chlorite-free serpentinized peridotites, talc crystallized in veins, or as a replacement for serpentine near these veins, as was also described by *Boschi et al.* [2006b] in samples from the Atlantis Massif (MAR, 30°N). These talc veins isolate angular clasts of serpentine, indicating that they formed by brittle failure of the serpentinized footwall of the fault (brittle deformation type 2; Figure 10). This brittle deformation was probably associated with high fluid pressures and hydrofracturing by a silica-rich hydrothermal fluid.

[55] Brittle failure of serpentine is, however, also observed in the talc-free or talc-poor polygenic breccia of DR3 (Ashadze; Figure 3e) and DR8 (Logatchev; Figures 2h and 4c) where there is no evidence for hydrofracturing. The serpentinized footwall next to the fault (Figure 10) was therefore at least locally subjected to stresses in excess of the yield brittle strength of serpentine. The recrystallization of chlorite and serpentine in shear zones between the serpentine clasts in the polygenic breccia (Figure 6f) suggests that plastic deformation at temperatures still within the greenschist facies field resumed after this higher stress brittle event. Similarly, in talc-rich samples, brittle failure of the serpentine was followed by plastic deformation in thin talc-bearing shear zones (Figures 6d and 6e). This succession of brittle failure followed by localized plastic deformation, at pressure and temperature conditions that were probably not very different, should not be forced into a simple model of a brittle lithosphere overlying a plastic lithosphere. Instead, it could be interpreted in the frame of a seismogenic fault zone and footwall.

[56] Available data on the seismicity of mid-ocean ridge detachment faults indicates sustained levels of low magnitude activity [*deMartin et al.*, 2007;

Escartín et al., 2008a; *Smith*, 2003]. The *deMartin et al.* [2007] study of seismicity next to the TAG detachment identified about 80 events per day, with magnitude between 1 and 4, at depths between 3 km below seafloor and the inferred base of the brittle lithosphere at about 8 km below seafloor. A recent study of seismicity in the area of the Logatchev vents indicates a similar pattern (I. Grevemeyer et al., personal communication, 2012). Based on our study of rock microstructures, we infer that the deepest seismic events could be due to brittle failure of the fresh peridotite (brittle deformation type 1). The other events may be due to brittle failure of serpentinized peridotites in the hydrothermally active fault zone and upper footwall. This may take the form of the rupture of a succession of small asperities in massive serpentinized peridotites along the main detachment fault zone or along associated secondary faults within the footwall. Where silica-rich fluids are abundant, serpentine clasts would be replaced by talc, which is weak and able to accommodate subsequent deformation aseismically by plastic creep (plastic to semi-brittle deformation 3; Figure 10). In the polygenic breccia samples from DR3 and DR8, talc replacement is minor, but brittle failure is followed by dynamic recrystallization of very fine-grained and well oriented chlorite and serpentine flakes (Figure 6f).

6.4. Can We Link the Diversity of Denudation Settings With Differences in the Lithology of the Fault and Footwall?

[57] In order to address the lithological differences that may exist between exhumed footwall rocks in the different regions of our study area, we must first face the limitations of dredging as a means to sample the seafloor geology. The length of our dredge tracks on the seafloor (from touch-down to off-bottom) ranges between 600 m and 2 km (Table 1). Samples in these dredges may have come from numerous locations along the track, or from only one decameter-scaled outcrop or talus deposit. The relative provenance of the different rock types in each dredge is therefore unconstrained: they may be juxtaposed at meter scale, or separated by distances of up to a few hundred meters. Nonetheless, the fact that we systematically find the three types of ultramafic lithologies (types 4a, b and c; Table 2) in our dredges (except for type 4a in DR1 but this is due to very extensive replacement of serpentine by talc in this dredge) is in favor of a distribution of these three rock types over short distances in the exhumed ultramafic seafloor. Similarly, the fact that we find gabbroic rocks in all dredges but DR5

(Table 2) also suggests that gabbroic rocks are interspersed in the ultramafic rocks at relatively short length scales (≤100 m). These inferred horizontal scales are consistent with the vertical scales of lithological heterogeneity documented in the IODP Leg 209 drill holes [*Kelemen et al.*, 2007; *Schroeder et al.*, 2007]. For example at site 1268, 3 intervals of gabbros, up to 20m-thick, are found in 140 m of serpentinized peridotites [*Kelemen et al.*, 2007].

[58] Another issue with dredges and ROV samples is that some lithologies, for example very uncohesive material may be systematically missed. We cannot rule this out and therefore base this discussion strictly on the deformations, and on the magmatic, and hydrothermal alteration events identified in our samples. Less cohesive fault rocks (gouge, cataclasites and serpentine schists), which would have been missed by our dredges, were for example reported from meter-thick low resistivity intervals in the serpentinized peridotites at IODP site 1272 [*Schroeder et al.*, 2007].

[59] In this study, we sampled only one location next to a fossil corrugated fault surface (DR1; Figure 1). In terms of lithologies (Table 2), samples from this location stand out by 1- the abundance of basaltic and metabasaltic lithologies, and 2- the greater relative abundance of amphibole-bearing serpentinized peridotites. The basalts in this dredge are unmetamorphosed lavas which presumably were either emplaced directly on the exhumed fault surface, or formed as rider blocks from the hanging wall. Metabasalts in DR1, however, are deformed and their protolith was thus intruded in the fault zone. This is very similar to the synkinematic diabase dikes described by *MacLeod et al.* [2002] in minicores drilled in the fossil corrugated surface at 15°45′N (MAR). Dredges in the large corrugated region south of the Kane Transform [*Dick et al.*, 2008] also recovered a significant proportion of metamorphic diabases. While the absence of this rock type in our dredges from the non-corrugated regions next to the Ashadze and Logatchev vents (DR3, DR5, DR6, DR7 and DR8; Table 2) may not be statistically robust, it is still worth noting. It suggests that domains of the footwall that had been cooled down to greenschist facies conditions were not, or not as commonly injected by melts at these non-corrugated locations.

[60] Ultramafic rocks in DR1 also contain a larger proportion of amphibole-bearing serpentinized peridotites (lithological type 4b) than the other dredges (Table 2): about 80% of the ultramafic

rocks recovered in dredge 1 belong to this lithology and we did not recover any talc and amphibole-free serpentinized peridotites (lithological type 4a). Again this is an indication for more sustained emplacement of gabbroic material next to the fault in the deeper and hotter domains next to the base of the brittle lithosphere (Figure 10).

[61] In terms of the sequence of deformation types (Table 3), ultramafic samples from dredge 1 are pervasively affected by plastic to semi-brittle deformation 2 (sheared tremolite), and display a more heterogeneous imprint of plastic to semi-brittle deformation 3 (sheared talc). The lack of fresh olivine in this dredge precluded the detection of plastic to semi-brittle deformation 1, but the angular shape of serpentine clasts in the amphibole-bearing samples (Figure 2b) suggests that they also underwent brittle deformation 1 (Figure 10). The overall deformation history of ultramafic rocks from DR1 appears therefore similar to that of our other dredges, as far as we can tell from the recovered samples. We may, however infer that due to their greater relative abundance, amphibole-bearing ultramafic rocks played a more effective role to accommodate fault displacements in the 750°–400°C temperature range in this corrugated surface context.

[62] DR3 and DR5, in the lower slopes of the axial valley wall at Ashadze (Figure 1), represent the opposite end-member in terms of the abundance of amphibole-bearing serpentinized peridotites, and of metagabbroic rocks: amphibole, chlorite and talc-free serpentinized peridotites represent over 80% in volume of the samples recovered in these dredges (Table 2). This indicates that these dredges sampled the footwall further away from a gabbroic intrusion. This could be either because gabbroic intrusions are heterogeneously distributed at a kilometer scale, or because detachment faulting there developed in a magma-starved context. The ultramafic samples from these dredges, and particularly the few amphibole-bearing samples, nonetheless display microstructural indicators for each of the deformation types identified in the other dredges (Table 3). This leads us to propose that these deformation types are indeed standard components of the deformation history of a MAR detachment fault.

[63] Ultramafic rocks from DR7 and DR8, coming from the non-corrugated hill above the Logatchev vents (Figure 1), also display microstructural indicators for each of the deformation types identified in our study (Table 3). These dredges represent

an intermediate case, with relatively abundant amphibole-bearing ultramafic rocks and gabbros, and about 30% amphibole and talc-free type 4a serpentinized peridotites (Table 2). DR8 contains a small proportion of unmetamorphosed basalts. It also contains about 20% in volume of polygenic ultramafic breccia, which we interpreted as formed from amphibole-bearing serpentinized peridotites during brittle 2 and plastic to semi-brittle 3 deformations. These two characteristics suggest that DR8, and thus also the nearby DR7, sampled the exhumed footwall not far beneath the actual exhumed fault surface. The hill sampled by DR7 and DR8 has a domal shape with slopes less than 20° toward and away from the axis (Figure 1). This suggests that in spite of the lack of visible corrugations, the exhumed fault and footwall probably underwent a large flexural rotation, as documented at other, corrugation-bearing, detachment fault locations [Garcés and Gee, 2007; MacLeod et al., 2011; Morris et al., 2009].

7. Conclusions

[64] We have described a set of 470 dredge and ROV samples collected from ultramafic and gabbroic outcrops in the footwall of axial detachments at 3 locations along the MAR (Figure 1). These samples come from a maximum of 500 m from the main fault at each location and comprise basalts, metabasalts, variably altered metagabbroic rocks, and ultramafic rocks. We further sorted the ultramafic samples into 3 lithological sub-types: serpentinized peridotites, amphibole $\pm$ chlorite-bearing serpentinized peridotites, and talc-bearing but amphibole and chlorite-free serpentinized peridotites.

[65] About 50% of these ultramafic samples display deformation microstructures which we have been able to relate to one or more of 3 types of plastic to brittle-plastic deformation, and 2 types of brittle deformation. Plastic to brittle-plastic deformation type 1 is mostly anhydrous, with dynamic recrystallization of olivine and pyroxenes at temperatures probably >800°C. Plastic to brittle-plastic deformation 2 is restricted to amphibole-bearing ultramafic samples and is controlled by deformation and syntectonic crystallization of tremolite at temperatures above the stability limit of serpentine (400°C). Finally, plastic to brittle-plastic deformation 3 postdates serpentinization and is accommodated by thin talc, or chlorite+serpentine $\pm$ talc shear zones. Brittle deformations affect either fresh peridotite (brittle deformation 1), or already serpentinized peridotite (brittle 2) and are associated in both cases with fluid injection: an evolved gabbroic melt for brittle deformation 1, and a Si-rich hydrothermal fluid for brittle deformation 2. Serpentinized peridotites injected by evolved gabbroic melts during brittle deformation 1 are the most likely protolith for the amphibole-bearing serpentinized peridotites. Keeping in mind that there may be a sampling bias against the most non-cohesive lithologies (such as gouges or serpentine schists), strain in the detachment footwall therefore appears to localize in shear zones made of minerals derived either from the hydrothermal alteration of a gabbroic+peridotite mixture (tremolite, chlorite), or from hydrothermal metasomatism of serpentinized peridotite (talc).

[66] While there are differences in the relative proportions basaltic, gabbroic and ultramafic rocks at the three locations sampled by our study, we find that the 3 ultramafic lithologies, and the 5 deformation types identified in our study are present at each location. This leads us to propose that they are representative of the lithologies and deformations in the ultramafic footwall next to MAR detachment faults. We conclude that the rheology of these faults is likely controlled both by the abundance of gabbroic injections at depth near the base of the brittle axial lithosphere, and by the pattern of hydrothermal circulations in the permeable domains in the fault and in its proximal footwall.

Acknowledgments

References

Andreani, M., C. Mevel, A. M. Boullier, and J. Escartín (2007), Dynamic control on serpentine crystallization in veins: Constraints on hydration processes in oceanic peridotites, *Geochem. Geophys. Geosyst.*, *8*, Q02012, doi:10.1029/2006GC001373.

Augustin, N., K. S. Lackschewitz, T. Kuhn, and C. W. Devey (2008), Mineralogical and chemical mass changes in mafic and ultramafic rocks from the Logatchev hydrothermal field (MAR 15°N), *Mar. Geol.*, *256*(1–1), 18–29, doi:10.1016/j.margeo.2008.09.004.

Batuev, B. N., A. G. Krotov, V. F. Markov, G. A. Cherkashev, and S. G. Krasnov (1994), Massive sulfide deposits discovered and sampled at 14°45′N, Mid-Atlantic Ridge, *BRIDGE Newsl.*, *6*, 6.

Bel'tenev, V., V. Ivanov, A. Shagin, M. Sergeyev, I. Rozhdestvenskaya, V. Shilov, I. Debretzova, G. Cherkashev, M. Samovarov, and I. Poroshina (2005), New hydrothermal

sites at 13 N, Mid-Atlantic Ridge, *InterRidge Newsl.*, *14*, 14–16.

Boschi, C., G. L. Früh-Green, A. Delacour, J. A. Karson, and D. S. Kelley (2006a), Mass transfer and fluid flow during detachment faulting and development of an oceanic core complex, Atlantis Massif (MAR 30°N), *Geochem. Geophys. Geosyst.*, *7*, Q01004, doi:10.1029/2005GC001074.

Boschi, C., G. L. Früh-Green, and J. Escartín (2006b), Occurrence and significance of serpentinite-hosted, talc-and amphibole-rich fault rocks in modern oceanic settings and ophiolite complexes: An overview, *Ofioliti*, *31*(2), 129–140.

Boudier, F., A. Baronnet, and D. Mainprice (2010), Serpentine mineral replacements of natural olivine and their seismic implications: Oceanic lizardite versus subduction-related antigorite, *J. Petrol.*, *51*(1–2), 495–512, doi:10.1093/petrology/egp049.

Bougault, H., J. L. Charlou, Y. Fouquet, H. D. Needham, N. Vaslet, P. Appriou, P. J. Baptiste, P. A. Rona, L. Dmitriev, and S. Silantiev (1993), Fast and slow spreading ridges: Structure and hydrothermal activity, ultramafic topographic highs, and CH4 output, *J. Geophys. Res.*, *98*(B6), 9643–9651, doi:10.1029/93JB00508.

Boyd, F. (1959), Hydrothermal investigations of amphiboles, in *Researches in Geochemistry*, pp. 377–396, John Wiley, New York.

Buck, W. R., L. L. Lavier, and A. N. B. Poliakov (2005), Modes of faulting at mid-ocean ridges, *Nature*, *434*(7034), 719–723, doi:10.1038/nature03358.

Cann, J., D. Blackman, D. Smith, E. McAllister, B. Janssen, S. Mello, E. Avgerinos, A. Pascoe, and J. Escartín (1997), Corrugated slip surfaces formed at ridge-transform intersections on the Mid-Atlantic Ridge, *Nature*, *385*(6614), 329–332, doi:10.1038/385329a0.

Cannat, M. (1996), How thick is the magmatic crust at slow spreading oceanic ridges?, *J. Geophys. Res.*, *101*(B2), 2847–2857, doi:10.1029/95JB03116.

Cannat, M., and J. F. Casey (1995), An ultramafic lift at the Mid-Atlantic Ridge: Successive stages of magmatism in serpentinized peridotites from the 15 N region, in *Mantle and Lower Crust Exposed in Oceanic Ridges and in Ophiolites*, pp. 5–34, Kluwer Acad., Dordrecht, Netherlands.

Cannat, M., D. Bideau, and H. Bougault (1992), Serpentinized peridotites and gabbros in the Mid-Atlantic Ridge axial valley at 15°37′N and 16°52′N, *Earth Planet. Sci. Lett.*, *109*(1–2), 87–106, doi:10.1016/0012-821X(92)90076-8.

Cannat, M., C. Mevel, M. Maia, C. Deplus, C. Durand, P. Gente, P. Agrinier, A. Belarouchi, G. Dubuisson, and E. Humler (1995), Thin crust, ultramafic exposures, and rugged faulting patterns at the Mid-Atlantic Ridge (22–24°N), *Geology*, *23*(1), 49–52, doi:10.1130/0091-7613(1995)023<0049:TCUEAR>2.3.CO;2.

Cannat, M., Y. Lagabrielle, H. Bougault, J. Casey, N. de Coutures, L. Dmitriev, and Y. Fouquet (1997), Ultramafic and gabbroic exposures at the Mid-Atlantic Ridge: Geological mapping in the 15°N region, *Tectonophysics*, *279*(1–4), 193–213, doi:10.1016/S0040-1951(97)00113-3.

Cannat, M., D. Sauter, V. Mendel, E. Ruellan, K. Okino, J. Escartin, V. Combier, and M. Baala (2006), Modes of seafloor generation at a melt-poor ultraslow-spreading ridge, *Geology*, *34*(7), 605–608, doi:10.1130/G22486.1.

Cannat, M., D. Sauter, J. Escartin, L. Lavier, and S. Picazo (2009), Oceanic corrugated surfaces and the strength of the axial lithosphere at slow spreading ridges, *Earth Planet. Sci. Lett.*, *288*, 174–183, doi:10.1016/j.epsl.2009.09.020.

Cannat, M., H. Ondréas, A. Mangeney, and Y. Fouquet (2010), Microbathymetry reveals landslides activity shaping the walls of the Mid-Atlantic axial valley, Abstract OS14A-08 presented at 2010 Fall Meeting, AGU, San Francisco, Calif., 13–17 Dec.

Ceuleneer, G., and M. Cannat (1997), High-temperature ductile deformation of Site 920 peridotites, *Proc. Ocean Drill. Program Sci. Results*, *153*, 23–34.

Charlou, J. L., J. P. Donval, C. Konn, H. Ondréas, Y. Fouquet, P. Jean-Baptiste, and E. Fourré (2010), High production and fluxes of H2 and CH4 and evidence of abiotic hydrocarbon synthesis by serpentinization un ultramafic-hosted hydrothermal systems on Mid-Atlantic Ridge, in *Diversity of Hydrothermal Systems on Slow Spreading Ocean Ridges*, *Geophys. Monogr. Ser.*, vol. 188, edited by P. Rona et al., pp. 265–296, AGU, Washington, D. C.

Cherkashov, G., V. Bel'tenev, V. Ivanov, L. Lazareva, M. Samovarov, V. Shilov, T. Stepanova, G. P. Glasby, and V. Kuznetsov (2008), Two new hydrothermal fields at the Mid-Atlantic Ridge, *Mar. Georesour. Geotechnol.*, *26*(4), 308–316, doi:10.1080/10641190802400708.

deMartin, B. J., R. A. Sohn, J. P. Canales, and S. E. Humphris (2007), Kinematics and geometry of active detachment faulting beneath the Trans-Atlantic Geotraverse (TAG) hydrothermal field on the Mid-Atlantic Ridge, *Geology*, *35*(8), 711, doi:10.1130/G23718A.1.

Dick, H. (1989), Abyssal peridotites, very slow spreading ridges and ocean ridge magmatism, in *Magmatism in the Ocean Basins*, *Geol. Soc. London Spec. Publ.*, *42*, 71–105.

Dick, H. J. B., J. Lin, and H. Schouten (2003), An ultraslow-spreading class of ocean ridge, *Nature*, *426*(6965), 405–412, doi:10.1038/nature02128.

Dick, H. J. B., M. A. Tivey, and B. E. Tucholke (2008), Plutonic foundation of a slow-spreading ridge segment: Oceanic core complex at Kane Megamullion, 23°30′N, 45°20′W, *Geochem. Geophys. Geosyst.*, *9*, Q05014, doi:10.1029/2007GC001645.

Dilek, Y., A. J. Coulton, and S. D. Hurst (1997), Serpentinization and hydrothermal veining in peridotites at site 920 in the Mark area, *Proc. Ocean Drill. Program Sci. Results*, *153*, 35–59.

Escartín, J., and M. Cannat (1999), Ultramafic exposures and the gravity signature of the lithosphere near the Fifteen-Twenty Fracture Zone (Mid-Atlantic Ridge, 14–16.5°N), *Earth Planet. Sci. Lett.*, *171*(3), 411–424, doi:10.1016/S0012-821X(99)00169-7.

Escartín, J., C. Mevel, C. MacLeod, and A. McCaig (2003), Constraints on deformation conditions and the origin of oceanic detachments: The Mid-Atlantic Ridge core complex at 15°45′N, *Geochem. Geophys. Geosyst.*, *4*(8), 1067, doi:10.1029/2002GC000472.

Escartín, J., D. K. Smith, J. Cann, H. Schouten, C. H. Langmuir, and S. Escrig (2008a), Central role of detachment faults in accretion of slow-spreading oceanic lithosphere, *Nature*, *455*(7214), 790–794, doi:10.1038/nature07333.

Escartín, J., M. Andreani, G. Hirth, and B. Evans (2008b), Relationships between the microstructural evolution and the rheology of talc at elevated pressures and temperatures, *Earth Planet. Sci. Lett.*, *268*(3–4), 463–475, doi:10.1016/j.epsl.2008b.02.004.

Francis, G. H. (1956), The serpentinite mass in Glen Urquhart, Inverness-shire, Scotland, *Am. J. Sci.*, *254*(4), 201, doi:10.2475/ajs.254.4.201.

Fujiwara, T., J. Lin, T. Matsumoto, P. B. Kelemen, B. E. Tucholke, and J. F. Casey (2003), Crustal Evolution of the

Mid-Atlantic Ridge near the Fifteen-Twenty Fracture Zone in the last 5 Ma, *Geochem. Geophys. Geosyst.*, *4*(3), 1024, doi:10.1029/2002GC000364.

Garcés, M., and J. S. Gee (2007), Paleomagnetic evidence of large footwall rotations associated with low-angle faults at the Mid-Atlantic Ridge, *Geology*, *35*(3), 279, doi:10.1130/G23165A.1.

Ghose, I., M. Cannat, and M. Seyler (1996), Transform fault effect on mantle melting in the MARK area (Mid-Atlantic Ridge south of the Kane transform), *Geology*, *24*(12), 1139, doi:10.1130/0091-7613(1996)024<1139:TFEOMM>2.3.CO;2.

Gràcia, E., J. L. Charlou, J. Radford-Knoery, and L. M. Parson (2000), Non-transform offsets along the Mid-Atlantic Ridge south of the Azores (38°N–34°N): Ultramafic exposures and hosting of hydrothermal vents, *Earth Planet. Sci. Lett.*, *177*(1–2), 89–103, doi:10.1016/S0012-821X(00)00034-0.

Grimes, C. B., B. E. John, M. J. Cheadle, F. K. Mazdab, J. L. Wooden, S. Swapp, and J. J. Schwartz (2009), On the occurrence, trace element geochemistry, and crystallization history of zircon from in situ ocean lithosphere, *Contrib. Mineral. Petrol.*, *158*(6), 757–783, doi:10.1007/s00410-009-0409-2.

Grimes, C. B., T. Ushikubo, B. E. John, and J. W. Valley (2011), Uniformly mantle-like δ18O in zircons from oceanic plagiogranites and gabbros, *Contrib. Mineral. Petrol.*, *161*(1), 13–33, doi:10.1007/s00410-010-0519-x.

Ildefonse, B., D. K. Blackman, B. E. John, Y. Ohara, D. J. Miller, C. J. MacLeod, and the Integrated Ocean Drilling Program Expeditions 304/305 Science Party (2007), Oceanic core complexes and crustal accretion at slow-spreading ridges, *Geology*, *35*(7), 623, doi:10.1130/G23531A.1.

Jöns, N., W. Bach, and T. Schroeder (2009), Formation and alteration of plagiogranites in an ultramafic-hosted detachment fault at the Mid-Atlantic Ridge (ODP Leg 209), *Contrib. Mineral. Petrol.*, *157*(5), 625–639, doi:10.1007/s00410-008-0357-2.

Karson, J., G. Thompson, S. Humphris, J. Edmond, W. Bryan, J. Brown, A. Winters, R. Pockalny, J. Casey, and A. Campbell (1987), Along-axis variations in seafloor spreading in the MARK area, *Nature*, *328*, 681–685.

Kelemen, P., T. Matsumoto, and S. S. Party (1998), Geological results of MODE 98, Leg 1: JAMSTEC/WHOI Shinkai 6500 Cruise to 15°N, Mid-Atlantic Ridge, *Eos Trans. AGU*, *79*(45), Fall Meet. Suppl., Abstract U22A-18.

Kelemen, P. B., E. Kikawa, D. J. Miller, and Shipboard Scientific Party (2007), *Proceedings of the Ocean Drilling Program: Scientific Results*, vol. 209, edited by P. B. Kelemen, E. Kikawa, and D. J. Miller, Ocean Drill. Program, College Station, Tex.

Koepke, J. (2005), Late stage magmatic evolution of oceanic gabbros as a result of hydrous partial melting: Evidence from the Ocean Drilling Program (ODP) Leg 153 drilling at the Mid-Atlantic Ridge, *Geochem. Geophys. Geosyst.*, *6*, Q02001, doi:10.1029/2004GC000805.

Koepke, J., J. Berndt, S. T. Feig, and F. Holtz (2007), The formation of SiO$_2$-rich melts within the deep oceanic crust by hydrous partial melting of gabbros, *Contrib. Mineral. Petrol.*, *153*(1), 67–84, doi:10.1007/s00410-006-0135-y.

Lavier, L. L., W. Roger Buck, and A. N. B. Poliakov (1999), Self-consistent rolling-hinge model for the evolution of large-offset low-angle normal faults, *Geology*, *27*(12), 1127, doi:10.1130/0091-7613(1999)027<1127:SCRHMF>2.3.CO;2.

Lavier, L. L., W. R. Buck, and A. N. B. Poliakov (2000), Factors controlling normal fault offset in an ideal brittle layer,

J. Geophys. Res., *105*(B10), 23,431–23,442, doi:10.1029/2000JB900108.

MacLeod, C. J., J. Escartín, D. Banerji, G. Banks, M. Gleeson, D. H. B. Irving, R. Lilly, A. McCaig, Y. Niu, and S. Allerton (2002), Direct geological evidence for oceanic detachment faulting: The Mid-Atlantic Ridge, 15°45′ N, *Geology*, *30*(10), 879–882, doi:10.1130/0091-7613(2002)030<0879:DGEFOD>2.0.CO;2.

MacLeod, C. J., R. C. Searle, B. J. Murton, J. F. Casey, C. Mallows, S. C. Unsworth, K. L. Achenbach, and M. Harris (2009), Life cycle of oceanic core complexes, *Earth Planet. Sci. Lett.*, *287*, 333–344, doi:10.1016/j.epsl.2009.08.016.

MacLeod, C. J., J. Carlut, J. Escartín, H. Horen, and A. Morris (2011), Quantitative constraint on footwall rotations at the 15°45′N oceanic core complex, Mid-Atlantic Ridge: Implications for oceanic detachment fault processes, *Geochem. Geophys. Geosyst.*, *12*, Q0AG03, doi:10.1029/2011GC003503.

McCaig, A. M., R. A. Cliff, J. Escartin, A. E. Fallick, and C. J. MacLeod (2007), Oceanic detachment faults focus very large volumes of black smoker fluids, *Geology*, *35*(10), 935–938, doi:10.1130/G23657A.1.

Mével, C., M. Cannat, P. Gente, E. Marion, J. Auzende, and J. Karson (1991), Emplacement of deep crustal and mantle rocks on the west median valley wall of the MARK area (MAR, 23° N), *Tectonophysics*, *190*(1), 31–53, doi:10.1016/0040-1951(91)90353-T.

Mitchell, N. C., M. A. Tivey, and P. Gente (2000), Seafloor slopes at mid-ocean ridges from submersible observations and implications for interpreting geology from seafloor topography, *Earth Planet. Sci. Lett.*, *183*(3–4), 543–555, doi:10.1016/S0012-821X(00)00270-3.

Morris, A., J. S. Gee, N. Pressling, B. E. John, C. J. MacLeod, C. B. Grimes, and R. C. Searle (2009), Footwall rotation in an oceanic core complex quantified using reoriented Integrated Ocean Drilling Program core samples, *Earth Planet. Sci. Lett.*, *287*(1–2), 217–228, doi:10.1016/j.epsl.2009.08.007.

Nicolas, A., and J. Poirier (1976), *Crystalline Plasticity and Solid-State Flow in Metamorphic Rocks*, John Wiley, New York.

O'Hanley, D. S. (1996), *Serpentinites: Records of Tectonic and Petrological History*, 34 pp., Oxford Univ. Press, New York.

Petersen, S., K. Kuhn, T. Kuhn, N. Augustin, R. Hékinian, L. Franz, and C. Borowski (2009), The geological setting of the ultramafic-hosted Logatchev hydrothermal field (14°45′N, Mid-Atlantic Ridge) and its influence on massive sulfide formation, *Lithos*, *112*(1–2), 40–56, doi:10.1016/j.lithos.2009.02.008.

Poirier, J. P. (1985), *Creep of Crystals: High-Temperature Deformation Processes in Metals, Ceramics, and Minerals*, Cambridge Univ. PressCambridge, U. K.

Rona, P., L. Widenfalk, and K. Boström (1987), Serpentinized ultramafics and hydrothermal activity at the Mid-Atlantic Ridge crest near 15°N, *J. Geophys. Res.*, *92*(B2), 1417–1427.

Schroeder, T., and B. E. John (2004), Strain localization on an oceanic detachment fault system, Atlantis Massif, 30°N, Mid-Atlantic Ridge, *Geochem. Geophys. Geosyst.*, *5*, Q11007, doi:10.1029/2004GC000728.

Schroeder, T., M. J. Cheadle, H. J. B. Dick, U. Faul, J. F. Casey, and P. B. Kelemen (2007), Nonvolcanic seafloor spreading and corner-flow rotation accommodated by extensional faulting at 15°N on the Mid-Atlantic Ridge: A structural synthesis of ODP Leg 209, *Geochem. Geophys. Geosyst.*, *8*, Q06015, doi:10.1029/2006GC001567.

Searle, R., P. Cowie, N. Mitchell, S. Allerton, C. MacLeod, J. Escartín, S. Russell, P. Slootweg, and T. Tanaka (1998),

Fault structure and detailed evolution of a slow spreading ridge segment: The Mid-Atlantic Ridge at 29° N, *Earth Planet. Sci. Lett.*, *154*(1–4), 167–183, doi:10.1016/S0012-821X(97)00160-X.

Silantyev, S. (1998), Origin conditions of the Mid-Atlantic Ridge plutonic complex at 13–17°N, *Petrology*, *6*(4), 351–387.

Silantyev, S. A., E. A. Krasnova, M. Cannat, N. S. Bortnikov, N. N. Kononkova, and V. E. Beltenev (2011), Peridotite-gabbro-trondhjemite association of the Mid-Atlantic Ridge between 12°58′ and 14°45′N: Ashadze and Logachev hydrothermal vent fields, *Geochem. Int.*, *49*(4), 323–354, doi:10.1134/S0016702911040070.

Smith, D. K. (2003), Spatial and temporal distribution of seismicity along the northern Mid-Atlantic Ridge (15°–35°N), *J. Geophys. Res.*, *108*(B3), 2167, doi:10.1029/2002JB001964.

Smith, D. K., J. R. Cann, and J. Escartin (2006), Widespread active detachment faulting and core complex formation near 13°N on the Mid-Atlantic Ridge, *Nature*, *442*(7101), 440–443, doi:10.1038/nature04950.

Smith, D. K., J. Escartin, H. Schouten, and J. R. Cann (2008), Fault rotation and core complex formation: Significant processes in seafloor formation at slow-spreading mid-ocean ridges (Mid-Atlantic Ridge, 13°–15°N), *Geochem. Geophys. Geosyst.*, *9*, Q03003, doi:10.1029/2007GC001699.

Tucholke, B. E., J. Lin, and M. C. Kleinrock (1998), Megamullions and mullion structure defining oceanic metamorphic core complexes on the Mid-Atlantic Ridge, *J. Geophys. Res.*, *103*(B5), 9857–9866, doi:10.1029/98JB00167.

Tucholke, B. E., M. D. Behn, W. R. Buck, and J. Lin (2008), Role of melt supply in oceanic detachment faulting and formation of megamullions, *Geology*, *36*(6), 455, doi:10.1130/G24639A.1.

Wicks, F. J. (1984), Deformation histories as recorded by serpentinites. III. Fracture patterns developed prior to serpentinization, *Can. Mineral.*, *22*, 205–209.